First-order performance evaluation of adaptive-optics systems for atmospheric-turbulence compensation in extended-field-of-view astronomical telescopes

Brent L. Ellerbroek

Starfire Optical Range, U.S. Air Force Phillips Laboratory, Kirtland Air Force Base, New Mexico 87117

Received August 7, 1992; accepted December 14, 1992; revised manuscript received January 19, 1993

An approach is presented for evaluating the performance achieved by a closed-loop adaptive-optics system that is employed with an astronomical telescope. This method applies to systems incorporating one or several guide stars, a wave-front reconstruction algorithm that is equivalent to a matrix multiply, and one or several deformable mirrors that are optically conjugate to different ranges. System performance is evaluated in terms of residual mean-square phase distortion and the associated optical transfer function. This evaluation accounts for the effects of the atmospheric turbulence $C_n^2(h)$ and wind profiles, the wave-front sensor and deformable-mirror fitting error, the sensor noise, the control-system bandwidth, and the net anisoplanatism for a given constellation of natural and/or laser guide stars. Optimal wave-front reconstruction algorithms are derived that minimize the telescope's field-of-view-averaged residual mean-square phase distortion. Numerical results are presented for adaptive-optics configurations incorporating a single guide star and a single deformable mirror, multiple guide stars and a single deformable mirror, or multiple guide stars and two deformable mirrors.

1. INTRODUCTION

The fact that laser-guide-star adaptive optics can dramatically improve the resolution of ground-based astronomical telescopes has been demonstrated experimentally.[1,2] The finite range of a laser guide star implies that the degree of turbulence compensation that is achieved decreases with increasing telescope-aperture diameter,[3,4] and the field of view (FOV) that is corrected by either a laser or a natural guide star is limited by the isoplanatic angle θ_0.[5] More sophisticated but undemonstrated approaches may overcome these limitations. The use of constellations of multiple laser guide stars has been suggested as a means of correcting atmospheric turbulence for large-aperture telescopes.[6,7] Adaptive-optics systems incorporating both multiple guide stars and multiple deformable mirrors may provide improved levels of turbulence compensation for FOV's that are larger than the isoplanatic patch.[8,9] Since the degree of atmospheric-turbulence correction that is desirable for astronomical imaging applications remains a subject of debate,[10] it is important that we accurately quantify the improvements in resolution that are feasible with more complex adaptive-optics systems.

In this paper an analysis technique is presented that is useful for evaluating and optimizing the performance of many advanced adaptive-optics concepts. A representative multiconjugate adaptive-optics configuration is illustrated in Fig. 1. In this system the wave fronts that are received from two laser and/or natural guide stars are measured with wave-front slope sensors that are optically conjugate to the telescope's primary mirror. The guide stars may be located at distinct ranges in one or several directions, and the wave-front slope sensors may differ in terms of subaperture geometry and measurement accuracy. Wave-front measurements that are obtained from laser guide stars cannot be used for overall tip–tilt correction because the position of the guide star is uncertain. The collection of all wave-front slope sensor measurements is combined into a single vector and is input into a wave-front reconstruction algorithm that is equivalent to a matrix multiply. The vector of deformable-mirror actuator adjustments that are produced as the output of this multiply is then temporally filtered by a servo control law before it is applied to one or several deformable mirrors. Each deformable mirror is characterized by a set of influence functions and is optically conjugate to a different range along the line of sight of the telescope. The intent of the figure adjustments that are finally applied to the deformable mirrors is to correct for turbulence-induced phase errors across the telescope's extended FOV.

The overall performance of the adaptive-optics control loop that is illustrated in Fig. 1 is determined by a wide range of parameters and error sources. The fitting error[11,12] is caused by the finite spatial resolution of the wave-front slope sensor subapertures and deformable-mirror actuators. Wave-front-sensor noise[13–15] propagates through the wave-front reconstruction algorithm and corrupts the figure adjustment that is applied to the deformable mirror. So-called servo lag results from the finite bandwidth of the control loop and limits the degree of correction that is achievable for time-varying wave-front distortions.[16,17] Anisoplanatic wave-front errors occur when wave-front measurements are recorded with a guide star that is displaced, either in range or in direction, from the object that is to be imaged.[7,5,17] It is important to consider the combined effect of these multiple error sources, since their integrated effect on overall adaptive-optics performance is frequently more forgiving than their independent values would suggest.[17] The techniques that are developed here provide integrated evaluations of the telescope's net optical transfer function (OTF) and the mean-square residual phase error that is induced by these four

0740-3232/94/020783-23$06.00

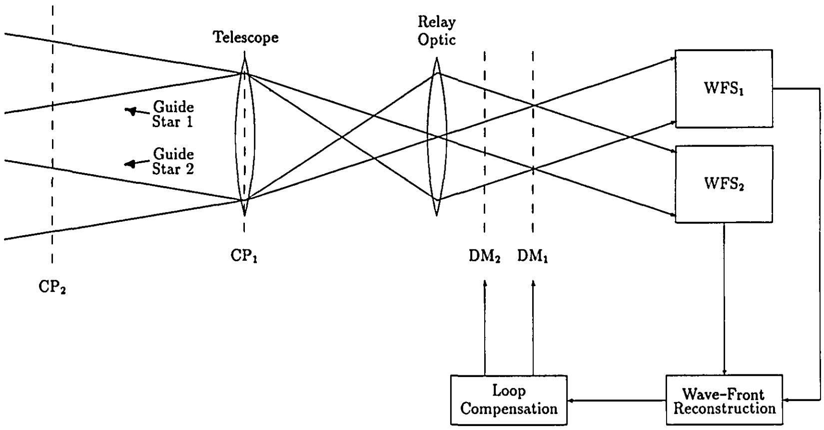

Fig. 1. Unfolded, foreshortened optical schematic of a multiconjugate adaptive-optics system with two guide stars and two deformable mirrors. CP_1 and CP_2 are the atmospheric layers that are conjugate to the deformable-mirror locations DM_1 and DM_2. WFS's, wave-front sensors.

error sources. Both quantities can be computed as a function of field angle for imaging telescopes with an extended FOV. We can optimize adaptive-optics performance by selecting wave-front reconstructor coefficients that minimize, subject to a constraint equation that is described below, the field-averaged, mean-square residual phase error that is due to residual atmospheric turbulence. Minimizing this value will, in general, maximize the field-averaged OTF of the telescope, but the relationship between the two quantities is nonlinear and is not always monotonic. Although it is integrated, the analysis remains first order in the sense that all the adaptive-optics components illustrated in Fig. 1 are treated as entirely linear. Turbulence-induced scintillation effects are also assumed to be negligible.

An important feature of the adaptive-optics configuration illustrated in Fig. 1 is the placement of the wave-front slope sensors relative to the deformable mirrors. Each wave-front slope sensor measures the net phase distortion along the path to its guide star after compensation by the current set of deformable-mirror figures. The actuator command vector that is computed by the wave-front reconstruction matrix is consequently an incremental adjustment that is to be summed with the current set of actuator commands. The closed-loop behavior of the adaptive-optics system is quite complex for an arbitrary set of wave-front reconstructor coefficients, and I was forced to introduce linear constraints on the coefficient values either to evaluate or to optimize adaptive-optics performance. Qualitatively, these constraints require the wave-front reconstructor to predict the current deformable-mirror actuator command vector correctly in the ideal case of no atmospheric turbulence or wave-front slope sensor noise. The least-squares estimator that is considered by Wallner[12] is an example of a reconstructor's satisfying this condition, but it is not the sole example. Standard optimization techniques can be used to determine the closed-loop reconstructor that will minimize the telescope's mean-square residual phase error subject to this constraint. Given the characteristics of actual wave-front sensors and deformable mirrors, accepting the closed-loop reconstructor constraint is prudent even if this constraint is not required by the analysis.

In Section 2 of this paper we develop our basic formulas for evaluating and optimizing adaptive-optics system performance. This derivation begins with a description of the Hilbert-space methods that are used to characterize the telescope's instantaneous mean-square residual phase distortion for a specific turbulence-induced phase profile and a specific set of deformable-mirror actuator commands. Subsection 2.B summarizes our first-order model for the wave-front reconstruction algorithm and the temporal dynamics of the adaptive-optics control loop. This linear model implies a highly nonlinear relationship between the reconstruction matrix coefficients and the control system's response to a particular time history of wave-front slope sensor measurements. Imposing closed-loop constraints on the wave-front reconstruction matrix linearizes this expression and yields a quadratic relationship between the reconstruction matrix and the adaptive-optics system's mean-square residual phase error. This quadratic formula can be used to evaluate the mean-square performance of any (constrained) reconstruction matrix and also to compute reconstructors that minimize the mean-square phase error that is subject to the required constraints.

Because the constrained wave-front reconstructor must precisely predict the deformable-mirror command vector in the hypothetical case of no atmospheric turbulence or wave-front slope sensor measurement noise, attempting to control poorly sensed deformable-mirror modes can degrade overall adaptive-optics system performance. Subsection 2.C describes how to identify these modes from the second-order statistics of the system's residual turbulence-induced phase error. The closed-loop constraints on the wave-front reconstruction matrix can then be modified to suppress control of these inaccurately sensed modes.

The models and results that are presented in Section 2 are expressed in terms of abstract deformable-mirror influence functions, wave-front slope sensor measurements, and turbulence-induced phase-distortion profiles. Geometric-optics models and computational formulas for these quantities are presented in Section 3. Subsection 3.A describes phase-distortion profiles and slope sensor measurements in terms of integrals over the atmosphere's turbulence-induced refractive-index profile. Optical deformable-mirror influence functions are then computed from these expressions, from the mirror's physical influence functions, and from the position of the deformable mirror within the telescope's optical train.

Subsection 3.C derives the second-order statistics of turbulence-induced phase profiles and wave-front slope sensor measurements as are required for the formulas of Section 2. These covariance matrices are computed for a Kolmolgorov turbulence spectrum with an infinite outer scale.

Section 4 presents sample numerical results that were computed for adaptive-optics systems of varying levels of complexity. Subsection 4.A parameterizes the effect of the fitting error and the wave-front-sensor noise for systems incorporating a single natural guide star and one deformable mirror that is conjugate to the telescope-aperture plane. Subsection 4.B evaluates the expected overall performance of representative single-guide-star systems. These cases have been selected to investigate the feasibility of compensating large-aperture astronomical telescopes at visible wavelengths under good seeing conditions. Subsection 4.C considers adaptive-optics systems with multiple guide stars but with only a single deformable mirror. The addition of a dim natural guide star or a high-altitude laser guide star can greatly enhance the performance of a system that is based on a single low-altitude laser guide star, even when this dim guide star is sensed with only a few large wave-front-sensor subapertures. Subsection 4.D considers a representative multiconjugate adaptive-optics configuration that employs two deformable mirrors and five natural and/or laser guide stars. Square FOV's as large as $5\theta_0$ in width can be well compensated with this sample system. Appendixes A and B discuss technical details of the derivations that are contained in Sections 2 and 3, and Appendix C summarizes the numerical integration techniques that were used to compute the results that are given in Section 4.

2. SYSTEM MODELS AND RESULTS

Figure 2 is a schematic control-system block diagram corresponding to the adaptive-optics system that is illustrated in Fig. 1. The input $\mathbf{y}(t)$ to this diagram is the open-loop vector of wave-front slope sensor measurements recorded at time t. This vector includes wave-front-sensor measurement noise and the effects of laser-guide-star position uncertainty but not the adjustment to the measured slopes that is caused by the current position of the deformable-mirror actuators. The closed-loop wave-front-sensor measurement vector that accounts for this effect is of the form $\mathbf{y}(t) - G\mathbf{c}(t)$, where $\mathbf{c}(t)$ is the deformable-mirror actuator command vector at time t and $G = \partial\mathbf{y}/\partial\mathbf{c}$ is the Jacobian matrix of first-order derivatives of $\mathbf{y}$ with respect to $\mathbf{c}$. The wave-front reconstruction algorithm operates on this closed-loop sensor vector and takes the form

$$\mathbf{e}(t) = M[\mathbf{y}(t) - G\mathbf{c}(t)], \tag{2.1}$$

where M is the matrix of wave-front reconstruction coefficients and $\mathbf{e}(t)$ is the vector of deformable-mirror actuator adjustments that are output by the reconstructor at time t. This vector of adjustments is temporally filtered before it is applied to the deformable mirror. A representative filter is given by the expression

$$\frac{d\mathbf{c}}{dt} = k\mathbf{e}(t), \tag{2.2}$$

where k is the gain of the filter in units of radians per second. Generalizations to this special case are considered below.[18]

The bottom third of Fig. 2 describes the degree of atmospheric-turbulence compensation that is achieved by the adaptive-optics system. The phase-distortion profile that is to be corrected is the function $\phi(\mathbf{x}, \boldsymbol{\theta})$ and is a function of both coordinates in the aperture plane $\mathbf{x}$ and of the point $\boldsymbol{\theta}$ within the telescope's FOV for which the distortion profile is evaluated. The residual phase-distortion profile $\epsilon(\mathbf{x}, \boldsymbol{\theta})$ that remains after the profile $\phi(\mathbf{x}, \boldsymbol{\theta})$ has been compensated by the telescope's deformable mirrors is de-

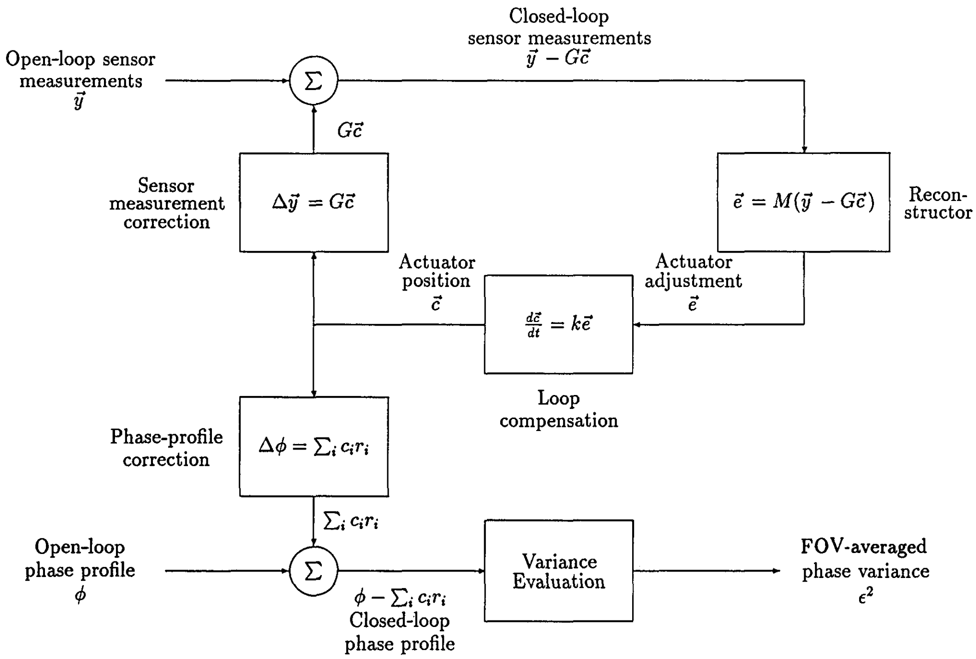

Fig. 2. Adaptive-optics system control-loop dynamics.

scribed by

$$\epsilon(\mathbf{x}, \boldsymbol{\theta}) = \phi(\mathbf{x}, \boldsymbol{\theta}) - \sum_i c_i r_i(\mathbf{x}, \boldsymbol{\theta}), \tag{2.3}$$

where $r_i(\mathbf{x}, \boldsymbol{\theta})$ is the influence function for the deformable-mirror influence function i. Since deformable mirrors may not be conjugate to the telescope's aperture plane, actuator influence functions are not, in general, independent of $\boldsymbol{\theta}$. The mean-square value of the residual profile $\epsilon(\mathbf{x}, \boldsymbol{\theta})$ with low-order modes removed will be abbreviated ϵ^2. The precise definition of ϵ^2 is given further below in this section.

The overall goal of this section is to evaluate the expected value of ϵ^2 for a given adaptive-optics control system and reconstruction matrix M and to determine reconstruction coefficients that will minimize this error.[19] Much of the development that is necessary for these results is most easily described in terms of Hilbert-space inner products and projection operators, and Subsection 2.A briefly reviews these concepts and introduces the associated notation. Subsection 2.B evaluates the closed-loop dynamics of the adaptive-optics control loop and demonstrates that obtaining a linear relationship between the coefficients of M and the deformable-mirror actuator command vector $\mathbf{c}(t)$ requires linear constraints on the reconstruction matrix M. These constraints are expressed in terms of an orthogonal projection operator Q operating on the vector space of deformable-mirror actuator commands. The resulting linear relationship between M and $\mathbf{c}(t)$ that is achieved with these constraints leads to the desired evaluation and minimization formulas for the residual mean-square phase error ϵ^2. Subsection 2.C describes how the constraints on reconstruction matrix coefficients may be adjusted to suppress the control of deformable-mirror modes that are inaccurately sensed and thus highly sensitive to wave-front slope sensor fitting error and measurement noise.

A. Hilbert-Space Preliminaries

The phase-distortion profile $\phi(\mathbf{x}, \boldsymbol{\theta})$ and the actuator influence function $r_i(\mathbf{x}, \boldsymbol{\theta})$ are both examples of real-valued, square-integrable functions that are defined on the space of pairs of points $(\mathbf{x}, \boldsymbol{\theta})$ from the telescope's aperture plane and FOV. The collection of all such functions is a vector space under the operations of pointwise addition and scalar multiplication. This vector space becomes a Hilbert space through the introduction of an inner product $[f, g]$ that is defined by

$$[f, g] = \int \mathrm{d}\boldsymbol{\theta} W_F(\boldsymbol{\theta}) \int \mathrm{d}\mathbf{x} W_A(\mathbf{x}) f(\mathbf{x}, \boldsymbol{\theta}) g(\mathbf{x}, \boldsymbol{\theta}). \tag{2.4}$$

Here $W_A(\mathbf{x})$ and $W_F(\boldsymbol{\theta})$ are two weighting functions that define the clear aperture and the FOV of the telescope. Note that the inner-product operation $[f, g]$ is linear in both of its arguments. It is convenient to assume that the functions $W_A(\mathbf{x})$ and $W_F(\boldsymbol{\theta})$ have been scaled to satisfy the conditions

$$\int \mathrm{d}\mathbf{x} W_A(\mathbf{x}) = 1, \tag{2.5}$$

$$\int \mathrm{d}\boldsymbol{\theta} W_F(\boldsymbol{\theta}) = 1. \tag{2.6}$$

The aperture weighting function $W_A(\mathbf{x})$ will be zero outside the clear aperture of the telescope and typically will be a single, constant value within this clear aperture. The FOV weighting function $W_F(\boldsymbol{\theta})$ may assume a broader range of values depending on the relative importance that the observer ascribes to different points in the telescope's FOV.

The input phase-distortion profile $\phi(\mathbf{x}, \boldsymbol{\theta})$ is defined only modulo an arbitrary constant. The aperture-averaged value of $\phi(\mathbf{x}, \boldsymbol{\theta})$ has no effect on the images that are produced by the telescope and should be nulled before evaluation of the adaptive-optics system performance in terms of the mean-square residual phase error ϵ^2. Additionally, the full-aperture tilt components of the function $\phi(\mathbf{x}, \boldsymbol{\theta})$ are not significant when the object of interest is smaller than the isoplanatic angle and bright enough to be imaged with short exposures. Both the piston-removed and the tilt-and-piston-removed phase-distortion profiles can be represented by

$$\tilde{\phi}(\mathbf{x}, \boldsymbol{\theta}) = \phi(\mathbf{x}, \boldsymbol{\theta}) - \sum_i f_i(\mathbf{x}) \int \mathrm{d}\mathbf{x}' W_A(\mathbf{x}') f_i(\mathbf{x}') \phi(\mathbf{x}', \boldsymbol{\theta}). \tag{2.7}$$

The functions $f_i(\mathbf{x})$ are the full-aperture piston mode and possibly the full-aperture tilt modes to be removed from the phase profile $\phi(\mathbf{x}, \boldsymbol{\theta})$. They are assumed to be scaled to satisfy the relationship

$$\int \mathrm{d}\mathbf{x} W_A(\mathbf{x}) f_i(\mathbf{x}) f_j(\mathbf{x}) = \begin{cases} 1 & \text{if } i = j \\ 0 & \text{otherwise} \end{cases}. \tag{2.8}$$

The notation $\tilde{\phi}$ is intended to suggest the higher-order component of the phase profile ϕ. Equation (2.7) can be abbreviated with operator notation in the form

$$\tilde{\phi} = P\phi. \tag{2.9}$$

Because of Eq. (2.8), the operator P is the orthogonal projection operator onto the subspace of functions with the full-aperture piston mode and possibly the full-aperture tilt modes removed. It may be verified that it satisfies the conditions $P^2 = P$ and $[Pf, g] = [f, Pg]$ for any two square-integrable functions f and g that are defined on the telescope's aperture and FOV.

In addition to turbulence-induced phase-distortion profiles, a second class of functions that are defined on pairs of points from the telescope's aperture and FOV are the phase corrections that are applied by the adaptive-optical system's deformable mirrors. By linearity, the correction that is applied for a given actuator command vector $\mathbf{c}$ is of the form $\Sigma_i c_i r_i(\mathbf{x}, \boldsymbol{\theta})$, where $r_i(\mathbf{x}, \boldsymbol{\theta})$ is the influence function corresponding to a unit adjustment to actuator i. This correction will also be abbreviated with operator notation in the form

$$(H\mathbf{c})(\mathbf{x}, \boldsymbol{\theta}) = \sum_i \mathbf{c}_i r_i(\mathbf{x}, \boldsymbol{\theta}). \tag{2.10}$$

It is natural to view the length and the direction of an actuator command vector $\mathbf{c}$ in terms of its effect on the phase-distortion profile $\phi(\mathbf{x}, \boldsymbol{\theta})$. This motivates us to define an inner product $[\mathbf{c}, \mathbf{c}']$ on the space of deformable-mirror actuator commands by

$$[\mathbf{c}, \mathbf{c}'] \equiv [PH\mathbf{c}, PH\mathbf{c}']. \tag{2.11}$$

The inner product appearing on the right-hand side of this definition has been defined in Eq. (2.4), and the quantities $PH\mathbf{c}$ and $PH\mathbf{c}'$ are the corrections obtained with the actuator command vectors $\mathbf{c}$ and $\mathbf{c}'$ with full-aperture piston removed and possibly full-aperture tilt removed. By once more invoking linearity, one can evaluate the inner product $[\mathbf{c}, \mathbf{c}']$ by using the expression

$$[\mathbf{c}, \mathbf{c}'] = \mathbf{c}^T R \mathbf{c}', \tag{2.12}$$

where $\mathbf{c}^T$ denotes the transpose of the vector $\mathbf{c}$ and the matrix R is defined by

$$\begin{aligned} R_{ij} &= [Pr_i, Pr_j] \\ &= \int \mathrm{d}\boldsymbol{\theta} W_F(\boldsymbol{\theta}) \int \mathrm{d}\mathbf{x} W_A(\mathbf{x}) \tilde{r}_i(\mathbf{x}, \boldsymbol{\theta}) \tilde{r}_j(\mathbf{x}, \boldsymbol{\theta}). \end{aligned} \tag{2.13}$$

This value for the matrix R generalizes previous definitions to the extended-FOV case.[7,12] Associated with the above inner product is a corresponding collection of projection operators. A matrix Q operating on the vector space of deformable-mirror actuator commands is an orthogonal projection operator for this inner product if it satisfies the conditions $Q^2 = Q$ and $[Q\mathbf{c}, \mathbf{c}'] = [\mathbf{c}, Q\mathbf{c}']$ for any pair of actuator command vectors $\mathbf{c}$ and $\mathbf{c}'$. The second condition is equivalent to the requirement that $Q^T R = RQ$.

The results of this research require that the actuator cross-coupling matrix R be positive definite so that the condition $\mathbf{c}^T R \mathbf{c} = 0$ implies that $\mathbf{c}$ must be the zero vector. This condition will not be satisfied in the usual case, in which the full-aperture piston and full-aperture tilt modes can be obtained as linear combinations of actuator influence functions. As in previous research,[12] the set of permissible deformable-mirror actuator command vectors must be restricted to a linear subspace for which the matrix R is positive definite. One possible subspace is obtained when we simply remove the required number of redundant degrees of freedom from the actuator command vector. A second subspace is the span of eigenvectors of R with positive eigenvalues. The range of phase profile corrections corresponding to these subspaces is identical, and the two choices are equivalent for the first-order analysis that is developed here.

The adaptive-optical system's mean-square residual phase error ϵ^2 may now be defined more precisely. The residual-phase-distortion profile $\epsilon(\mathbf{x}, \boldsymbol{\theta})$ itself may be abbreviated in the form

$$\epsilon = \phi - H\mathbf{c}, \tag{2.14}$$

and the mean-square value of ϵ with the full-aperture piston mode and possibly the full-aperture tilt modes removed is simply

$$\epsilon^2 = [P\epsilon, \mathrm{P}\epsilon]. \tag{2.15}$$

The utility of the above Hilbert-space formalism will become apparent in the equations that are developed below to evaluate and to minimize the expected value of ϵ^2.

B. Evaluating and Optimizing Closed-Loop Adaptive-Optics Performance

It follows from Eqs. (2.1) and (2.2) that the steady-state closed-loop performance of the adaptive-optics control loop for a specified time history $\mathbf{y}(t)$ of open-loop wave-front slope sensor measurements is given by

$$\mathbf{c}(t) = \int_0^\infty \mathrm{d}\tau\, k \exp(-k\tau MG) M \mathbf{y}(t - \tau). \tag{2.16}$$

Adaptive-optics system performance is a nonlinear function of the wave-front reconstruction matrix M. It appears to be difficult to proceed beyond Eq. (2.16) either to evaluate or to optimize expected adaptive-optics system performance in this general case.

Equation (2.16) can be simplified to a more useful expression by the imposition of linear constraints on the reconstruction matrix M. These constraints are the equalities

$$MG = Q, \tag{2.17}$$

$$QM = M, \tag{2.18}$$

where the matrix Q is the orthogonal projection operator onto a given linear subspace of the space of deformable-mirror actuator commands. These two constraints are equivalent to the following qualitative requirements:

- The range space of M is contained within the range space of Q [Eq. (2.18)],
- Actuator command vectors within the range space of Q are estimated precisely by the reconstructor in the absence of wave-front-sensor noise and atmospheric turbulence [Eq. (2.17)], and
- Actuator command vectors that are orthogonal to the range space of Q yield the zero vector as reconstructor output [Eq. (2.17)].

The projection operator Q and the associated actuator command subspace that are selected for the above constraints are arbitrary for the present discussion. In Subsection 2.C we describe how to select a projection operator Q to optimize adaptive-optics system performance.

Recall from Subsection 2.A that any orthogonal projection operator Q satisfies the condition $Q^2 = Q$. Taken together, the relationships $Q^2 = Q$, $MG = Q$, and $QM = M$ imply the simplification

$$\begin{aligned} \exp(-k\tau MG)M &= \exp(-k\tau Q)M \\ &= \left[\sum_{i=0}^{\infty} \frac{(-k\tau Q)^i}{i!}\right] M \\ &= QM \sum_{i=0}^{\infty} \frac{(-k\tau)^i}{i!} \\ &= M \exp(-k\tau). \end{aligned} \tag{2.19}$$

Substituting this formula into Eq. (2.16) yields

$$\mathbf{c}(t) = M\mathbf{s}(t), \tag{2.20}$$

where the vector $\mathbf{s}(t)$ is defined by

$$\mathbf{s}(t) = \int_0^\infty \mathrm{d}\tau\, k \exp(-k\tau) \mathbf{y}(t - \tau). \tag{2.21}$$

The vector $\mathbf{s}(t)$ is the convolution of the open-loop wave-front slope sensor vector $\mathbf{y}(t)$ with the closed-loop impulse-response function of a single-input, single-output control system described by scalar-valued analogs of Eqs. (2.1) and (2.2). This conclusion holds if Eq. (2.2) is replaced by any ordinary differential equation with constant coefficients.

Equation (2.20) provides a linear relationship between wave-front reconstructor coefficients and closed-loop actuator commands. The form of this relationship is similar to that of the open-loop case that was previously evaluated.[7,12] Substituting Eqs. (2.14) and (2.20) into Eq. (2.15) yields

$$\begin{aligned}\epsilon^2 &= [P(\phi - HM\mathbf{s}), P(\phi - HM\mathbf{s})] \\ &= [P\phi, P\phi] - 2\sum_{i,j}[P\phi, Pr_i]M_{ij}s_j + \sum_{i,j}\sum_{i',j'}R_{ii'}M_{ij}M_{i'j'}s_js_{j'}\end{aligned} \qquad (2.22)$$

for the instantaneous value of the field-averaged mean-square residual phase error ϵ^2. One obtains the second equality by using the linearity of the inner product. The ensemble-averaged value of ϵ^2 may now be written in the form

$$\langle\epsilon^2\rangle = \langle{\epsilon_0}^2\rangle - 2\sum_{i,j}M_{ij}A_{ij} + \sum_{i,j}\sum_{i',j'}R_{ii'}M_{ij}M_{i'j'}S_{jj'}, \qquad (2.23)$$

where $\langle\,\rangle$ represents ensemble averaging over the statistics of phase-distortion profiles $\phi(\mathbf{x}, \boldsymbol{\theta})$ and wave-front slope sensor measurements $\mathbf{s}$ and the quantities $\langle{\epsilon_0}^2\rangle$, A, and S are defined by

$$\langle{\epsilon_0}^2\rangle = \langle[P\phi, P\phi]\rangle, \qquad (2.24)$$

$$A_{ij} = \langle[P\phi, Pr_i]s_j\rangle, \qquad (2.25)$$

$$S_{ij} = \langle s_is_j\rangle. \qquad (2.26)$$

This notation was again selected to conform with previous results.[7,12] Assuming that the quantities A, S, R, and $\langle{\epsilon_0}^2\rangle$ have been computed for a given adaptive-optics configuration and a given set of atmospheric-turbulence statistics, Eq. (2.23) may be used to evaluate the expected performance of any wave-front reconstruction matrix M that satisfies the constraints given by Eqs. (2.17) and (2.18).

Equation (2.23) for the expected mean-square residual phase error $\langle\epsilon^2\rangle$ is quadratic in the coefficients of the reconstruction matrix M, and the constraints on M that are imposed by Eqs. (2.17) and (2.18) are linear. The value of M that minimizes $\langle\epsilon^2\rangle$ subject to the specified constraints can be determined with Lagrange multiplier techniques. The constrained minimum-variance reconstructor must satisfy the relationship

$$-A_{ij} + \sum_{i',j'}M_{i'j'}R_{ii'}S_{jj'} = \sum_{j'}\lambda_{jj'}G_{jj'} + \sum_{i'}\gamma_{i'j}(Q - I)_{i'i}, \qquad (2.27)$$

where I is the identity matrix. In matrix notation this relationship becomes

$$-A + RMS = \Lambda G^T + (Q^T - I)\Gamma. \qquad (2.28)$$

Solving Eqs. (2.17), (2.18), and (2.28) yields

$$M = Q[R^{-1}AS^{-1} + (I - R^{-1}AS^{-1}G)(G^TS^{-1}G)^{-1}G^TS^{-1}] \qquad (2.29)$$

for the constrained minimal-variance wave-front reconstructor.[20] One may then determine the minimized mean-square field-averaged residual phase error by substituting this value of M back into Eq. (2.23).

Equation (2.29) for M uses the assumption that the actuator cross-coupling matrix R is invertible. The first term within the brackets in Eq. (2.29) is similar to the formula for the minimal-variance reconstructor in the open-loop unconstrained case,[7,12] but the definitions of the matrices S and A are subtly different. The second term within the brackets guarantees that the constraint in Eq. (2.17) is observed, and the factor Q ensures that Eq. (2.18) is also satisfied.

C. Optimizing the Reconstructor Range Space

One constraint that is imposed on the closed-loop wave-front reconstruction matrix M is that it must correctly estimate all deformable-mirror actuator command vectors within a specified subspace in the absence of wave-front-sensor noise and atmospheric turbulence. This constraint may degrade adaptive-optics system performance if some actuator command modes in this subspace are poorly sensed because of wave-front-sensor noise or anisoplanatism. In this case it is desirable to reduce the range space of the wave-front reconstruction matrix to avoid inaccurately sensed modes. Formulas for identifying such modes and for removing them from the reconstructor's range space are developed presently.

For this derivation it is convenient to rewrite Eq. (2.23) for the expected mean-square residual phase error $\langle\epsilon^2\rangle$ in the matrix form

$$\langle\epsilon^2\rangle = \langle{\epsilon_0}^2\rangle - \mathrm{tr}(MA^T + AM^T - MSM^TR). \qquad (2.30)$$

Here $\mathrm{tr}(V)$ denotes the trace of a square matrix V. The following discussion will frequently use the identity

$$\mathrm{tr}(UV^T) = \mathrm{tr}(V^TU), \qquad (2.31)$$

which is valid for any two matrices V and U of common dimensions. This identity permits Eq. (2.30) to be rewritten as

$$\langle\epsilon^2\rangle = \langle{\epsilon_0}^2\rangle - \mathrm{tr}(BR), \qquad (2.32)$$

where the matrix B is defined by

$$B = MA^TR^{-1} + R^{-1}AM^T - MSM^T. \qquad (2.33)$$

The matrix B is symmetric. It follows that the matrix $R^{1/2}BR^{1/2}$ is also symmetric[21] and admits of an eigenvector–eigenvalue decomposition of the form

$$R^{1/2}BR^{1/2} = O^T\Lambda O. \qquad (2.34)$$

The matrix O of orthonormal eigenvectors satisfies the relationship

$$OO^T = O^TO = I, \qquad (2.35)$$

and the matrix Λ is a diagonal matrix consisting of the eigenvalues of $R^{1/2}BR^{1/2}$:

$$\Lambda = \mathrm{diag}(\lambda_1, \ldots, \lambda_n). \qquad (2.36)$$

Invoking Eqs. (2.31) and (2.35) yields

$$\begin{aligned}\langle\epsilon^2\rangle &= \langle{\epsilon_0}^2\rangle - \mathrm{tr}(BR)\\ &= \langle{\epsilon_0}^2\rangle - \mathrm{tr}(O^T\Lambda O)\\ &= \langle{\epsilon_0}^2\rangle - \mathrm{tr}(OO^T\Lambda)\\ &= \langle{\epsilon_0}^2\rangle - \mathrm{tr}(\Lambda)\end{aligned}\tag{2.37}$$

for the value of the expected mean-square residual phase error $\langle\epsilon^2\rangle$. The net effect of the adaptive-optics control system is to reduce the telescope's mean-square phase error by the trace of the matrix Λ. Controlling deformable-mirror actuator command modes with negative eigenvalues λ_i increases the value of $\langle\epsilon^2\rangle$.

We can improve adaptive-optics system performance by reducing the range of the wave-front reconstruction matrix M to a new subspace that is orthogonal to all the eigenvectors of the matrix $R^{1/2}BR^{1/2}$ that have negative eigenvalues. This subspace is the range of the orthogonal projection operator $Q*$, defined by the formulas

$$l_i = \begin{cases}0 & \text{if } \lambda_i \le 0\\ 1 & \text{otherwise}\end{cases},\tag{2.38}$$

$$L = \mathrm{diag}(l_1, \ldots, l_n),\tag{2.39}$$

$$Q* = R^{-1/2}O^TLOR^{1/2}.\tag{2.40}$$

The associated reconstructor $M*$ is defined as

$$M* = Q*M.\tag{2.41}$$

Before evaluating the new mean-square residual phase error $\langle\epsilon^2\rangle$ for the reconstruction matrix $M*$ we must verify that the matrix $Q*$ is indeed an orthogonal projection operator and that the reconstructor $M*$ satisfies the constraints that are given in Eqs. (2.17) and (2.18), with the projection operator Q being replaced by $Q*$. To be an orthogonal projection operator, the matrix $Q*$ must satisfy the conditions

$$Q*^2 = Q*,\tag{2.42}$$

$$Q*^TR = RQ*.\tag{2.43}$$

These relationships follow immediately from Eq. (2.35) and the definition of $Q*$. Together, Eqs. (2.41) and (2.42) yield the relationship $Q*M* = Q*Q*M = Q*M = M*$, which is the equivalent of Eq. (2.18) for the reconstruction matrix $M*$. Appendix A derives the result $Q*Q = Q*$, which, when combined with Eqs. (2.41) and (2.17), yields $M*G = Q*MG = Q*Q = Q*$. This is the analog of Eq. (2.17) for the reconstructor $M*$ and is the last result that is necessary for verification that the matrices $M*$ and $Q*$ satisfy the required conditions.

Substituting the reduced range reconstructor $M*$ for M in Eq. (2.30) results in the expression

$$\begin{aligned}\langle\epsilon^2\rangle &= \langle{\epsilon_0}^2\rangle - \mathrm{tr}(M*A^T + AM*^T - M*SM*^TR)\\ &= \langle{\epsilon_0}^2\rangle - \mathrm{tr}[O^TLOR^{1/2}(MA^TR^{-1} + R^{-1}AM^T\\ &\quad - MSM^T)R^{1/2}]\\ &= \langle{\epsilon_0}^2\rangle - \mathrm{tr}(O^TLOO^T\Lambda O)\\ &= \langle{\epsilon_0}^2\rangle - \mathrm{tr}(L\Lambda)\end{aligned}\tag{2.44}$$

for the expected mean-square residual phase error $\langle\epsilon^2\rangle$. By Eq. (2.39), the trace of the matrix $L\Lambda$ is the sum of the positive eigenvalues λ_i. The range space of the modified reconstructor $M*$ is orthogonal to all inaccurately sensed modes that would degrade the time-averaged performance of the adaptive-optics control loop.

3. COMPONENT MODELS AND EVALUATION FORMULAS

The adaptive-optics evaluation and optimization formulas that are developed above are for an abstract adaptive-optics system. These results are expressed in terms of matrices depending on deformable-mirror influence functions (G, R, and A), wave-front slope sensor subaperture geometries (S, A, and G), and the statistics of atmospheric turbulence and sensor noise (S and A). This section derives evaluation formulas that describe these matrices for specific adaptive-optics configurations. The results that are obtained are applicable for either a Hartmann sensor or a shearing interferometer, either a continuous deformable mirror or a segmented mirror, and a variety of wave-front-sensor-subaperture deformable-mirror-actuator configurations.[15,22] All the results, however, are based on first-order models for these components that neglect diffraction effects. For a Hartmann sensor this assumption does not apply if the wave-front distortions within individual subapertures are large enough to aberrate the subaperture guide-star images significantly. The linearity of a shearing interferometer wave-front sensor is also degraded by large wave-front distortions within individual subapertures unless the shear width is kept small relative to the atmospheric-turbulence correlation length. Either sensor is susceptible to so-called 2π ambiguities if it is used with a segmented mirror and monochromatic light.

Subsection 3.A reviews standard first-order formulas for turbulence-induced phase-distortion profiles and wave-front slope sensor measurements. Both quantities are represented in a common form to simplify the computational expressions for the covariance matrices S and A. The formulas for slope sensor measurements reflect the effect of laser-guide-star position uncertainty. Subsection 3.B expresses the actuator optical influence functions $r_i(\mathbf{x}, \boldsymbol{\theta})$ and the associated matrices R and G in terms of actuator physical influence functions, the position of the deformable mirror within the telescope's optical train, and the range and the direction of each guide star. Subsection 3.C contains a detailed derivation of evaluation formulas for the covariance matrices S and A. These expressions are for the case of the Kolmogorov turbulence spectrum, for specified atmospheric turbulence ${C_n}^2(h)$ and wind-speed profiles, and for random, uniformly distributed wind directions at each altitude.

A. Wave-Front and Wave-Front-Sensor Models

The turbulence-induced phase-distortion profile in which the piston mode and possibly the tilt modes have been removed, $\tilde{\phi}(\mathbf{x}, \boldsymbol{\theta}, t)$, is defined in Section 2 by

$$\tilde{\phi}(\mathbf{x}, \boldsymbol{\theta}, t) = \phi(\mathbf{x}, \boldsymbol{\theta}, t) - \sum_i f_i(\mathbf{x}) \int \mathrm{d}\mathbf{x}' W_A(\mathbf{x}') f_i(\mathbf{x}') \phi(\mathbf{x}', \boldsymbol{\theta}, t).\tag{3.1}$$

Recall that $\mathbf{x}$ is a point in the aperture plane of the telescope, $\boldsymbol{\theta}$ is a point in the telescope's FOV, the functions $f_i(\mathbf{x})$ are the orthonormal piston mode and possibly the orthonormal tilt modes that are to be removed from the phase profile, and $W_A(\mathbf{x}')$ is the aperture function of the telescope. Our model for $\phi(\mathbf{x}, \boldsymbol{\theta}, t)$, the phase-distortion profile that includes low-order modes, assumes that the strength and the distribution of atmospheric turbulence are such that diffraction and scintillation effects can be neglected. The phase distortion that is encountered by a ray as it propagates from the direction $\boldsymbol{\theta}$ to the point in the aperture plane with coordinates $\mathbf{x}$ is given by the integral

$$\phi(\mathbf{x}, \boldsymbol{\theta}, t) = \frac{2\pi}{\lambda} \int_0^{z_0} \mathrm{d}z\, n(\mathbf{x} + z\boldsymbol{\theta}, z, t). \tag{3.2}$$

Here λ is the wavelength of the light, z denotes the range along the optical axis of the telescope, and $n(\mathbf{x}, z, t)$ is the turbulence-induced variation in the refractive index of the atmosphere at range z, at transverse coordinates $\mathbf{x}$, and at time t. Equation (3.2) implicitly introduces the paraxial approximation $\sin(\theta) = \theta$ for the magnitude of all angles $\boldsymbol{\theta}$ within the telescope's FOV. The assumed temporal dynamics of the refractive-index profile $n(\mathbf{x}, z, t)$ are based on the Taylor hypothesis:

$$n(\mathbf{x}, z, t) = n_0(\mathbf{x} - t\mathbf{v}, z), \tag{3.3}$$

where $\mathbf{v}$ is the transverse velocity vector of the wind at range z and $n_0(\mathbf{x}, z)$ is the refractive-index profile at time $t = 0$. The upper bound of integration z_0 in Eq. (3.2) can be any range that is greater than the limit of atmospheric turbulence. For purposes of this paper it is convenient to assume that this integration limit is significantly greater, so the separation between the points $\mathbf{x} + z\boldsymbol{\theta}$ and $[1 - (z/z_0)]\mathbf{x} + z\boldsymbol{\theta}$ is negligible for all points $\mathbf{x}$ within the telescope aperture and all ranges z within the atmosphere.

One must know the distribution of the wind-velocity vector $\mathbf{v}$ and the second-order statistics of the refractive-index profile n_0 to calculate the covariance matrices A and S. For isotropic Kolmogorov turbulence with a zero inner scale and an infinite outer scale, the power spectrum Φ_n of refractive-index variations is given by[23]

$$\begin{aligned}\Phi_n(\kappa, z) &\equiv \langle |\hat{n}_0(\boldsymbol{\kappa}, z)|^2 \rangle \\ &= 9.69 \times 10^{-3} C_n^2(z) \kappa^{-11/3},\end{aligned} \tag{3.4}$$

where κ is the spatial wave number, $\hat{n}_0(\boldsymbol{\kappa}, z)$ is the Fourier transform of $n_0(\mathbf{x}, z)$ with respect to $\mathbf{x}$, and $C_n^2(z)$ is the refractive-index structure function at range z. In this paper we assume that the wind speed v is a fixed, known function of altitude and that the direction of the wind is a uniformly distributed random variable in the coordinate system of the telescope aperture. The latter condition will be satisfied regardless of the geographical wind direction if performance predictions are averaged over all possible orientations of the telescope's azimuth gimbal.

The vector $\mathbf{s}(t)$ of temporally filtered wave-front slope sensor measurements will also be modeled with geometric-optics approximations. Recall from Section 2 that this vector is defined by the integral

$$\mathbf{s}(t) = \int_0^\infty \mathrm{d}\tau\, k \exp(-k\tau) \mathbf{y}(t - \tau), \tag{3.5}$$

where $\mathbf{y}$ is the instantaneous wave-front slope sensor measurement vector and k is the bandwidth of the adaptive-optics control loop in radians per unit time. Each component of the vector $\mathbf{y}$ is a noisy wave-front slope sensor measurement of the wave-front that is received from either a natural or a laser guide star. For a natural guide star this measurement is modeled as the average tilt of the wave front over a particular wave-front-sensor subaperture. Tilt measurements from laser guide stars are modeled similarly, except that the angular position error of the guide star, because of its projection through atmospheric turbulence, must be subtracted from the subaperture-averaged wave-front slope. Either case may be represented by an expression of the form

$$y_i(t) = \int \mathrm{d}\mathbf{x} W_i^s(\mathbf{x}) \phi^i(\mathbf{x}, t) + \alpha_i(t), \tag{3.6}$$

where α_i is the additive noise that is included in the measurement, $\phi^i(\mathbf{x}, t)$ is the wave front that is received from the guide star, and $W_i^s(\mathbf{x})$ is a distribution representing a line integral in the aperture plane of the telescope. For a natural guide star the path of this line integral is around the boundary of the given subaperture.[24] For a laser guide star a second line integral around the boundary of the illuminator's projection aperture must be included in the definition of $W_i^s(\mathbf{x})$ to account for guide-star position error. The noise term $\alpha_i(t)$ is assumed to be temporally white and uncorrelated between separate guide stars and subapertures. Its second-order statistics are described by

$$\langle \alpha_i(t) \alpha_{i'}(t') \rangle = \delta_{ii'} \delta(t - t') P_i. \tag{3.7}$$

The wave fronts $\phi^i(\mathbf{x}, t)$ that are received from each guide star are modeled geometrically by

$$\phi^i(\mathbf{x}, t) = \frac{2\pi}{\lambda} \int_0^{z_i} \mathrm{d}z n \left[\mathbf{x} + \left(\frac{z}{z_i} \right) (\mathbf{p}^i - \mathbf{x}), z, t \right], \tag{3.8}$$

where z_i is the range to the guide star and $\mathbf{p}^i$ is the coordinate of the guide star in the plane that is perpendicular to the telescope's line of sight.

It is convenient to combine Eqs. (3.1) and (3.2) for the phase-distortion profile $\tilde{\phi}(\mathbf{x}, \boldsymbol{\theta}, t)$ and Eqs. (3.5), (3.6), and (3.8) for the slope sensor measurement $s_i(t)$ into a common representation. This representation is the triple integral

$$\begin{aligned}u = \int_0^\infty \mathrm{d}\tau w(\tau) \Bigg\{ \int \mathrm{d}\mathbf{x}' v(X') \left(\frac{2\pi}{\lambda} \right) \\ \times \int_0^{z_i} \mathrm{d}\zeta n \left[\mathbf{x}' + \left(\frac{\zeta}{z_i} \right) (\mathbf{p} - \mathbf{x}'), \zeta, t - \tau \right] + \alpha(t - \tau) \Bigg\}.\end{aligned} \tag{3.9}$$

The generalized temporal weighting function $w(\tau)$, the aperture weighting function $v(\mathbf{x}')$, the wave-front source coordinate $\mathbf{p}$, and the noise term α are defined by

$$w(\tau) = \begin{cases} \delta(\tau) & \text{if } u = \tilde{\phi}(\mathbf{x}, \boldsymbol{\theta}, t) \\ k \exp(-k\tau) & \text{if } u = s_i(t) \end{cases}, \tag{3.10}$$

$$v(\mathbf{x}') = \begin{cases} W_A(\mathbf{x}')\left[\delta(\mathbf{x} - \mathbf{x}') - \sum_i f_i(\mathbf{x}) f_i(\mathbf{x}')\right] & \text{if } u = \tilde{\phi}(\mathbf{x}, \boldsymbol{\theta}, t) \\ W_i^s(\mathbf{x}') & \text{if } u = s_i(t) \end{cases}, \tag{3.11}$$

$$\mathbf{p} = \begin{cases} z_0 \boldsymbol{\theta} & \text{if } u = \tilde{\phi}(\mathbf{x}, \boldsymbol{\theta}, t) \\ \mathbf{p}^i & \text{if } u = s_i(t) \end{cases}, \tag{3.12}$$

$$\alpha(\tau) = \begin{cases} 0 & \text{if } u = \tilde{\phi}(\mathbf{x}, \boldsymbol{\theta}, t) \\ \alpha_i(\tau) & \text{if } u = s_i(t) \end{cases}. \tag{3.13}$$

Equation (3.12) invokes the assumption that the separation between the points $\mathbf{x} + z\boldsymbol{\theta}$ and $[1 - (z/z_0)]\mathbf{x} + z\boldsymbol{\theta}$ is negligible for all points $\mathbf{x}$ in the telescope aperture and ranges z within the atmosphere. Note for our discussion below that both possible definitions of the function $v(\mathbf{x})$ that are given in Eq. (3.11) satisfy the condition

$$\int \mathrm{d}\mathbf{x}\, v(\mathbf{x}) = 0. \tag{3.14}$$

The aperture weighting function $v(\mathbf{x})$ should not be confused with the wind-velocity vector $\mathbf{v}$.

B. Deformable-Mirror Models

As is illustrated in Fig. 1, each deformable mirror in the adaptive-optics system is optically conjugate to a plane in the atmosphere at some range from the aperture of the telescope. Let this range be denoted d_i for the deformable-mirror actuator i, and let the function $h_i(\mathbf{x})$ represent the physical influence function of this actuator imaged onto the conjugate plane. The optical influence function for actuator i will be modeled by

$$r_i(\mathbf{x}, \boldsymbol{\theta}) = h_i(\mathbf{x} + d_i\boldsymbol{\theta}). \tag{3.15}$$

This equation assumes the paraxial approximation $\sin(\theta) = \theta$ for all angles $\boldsymbol{\theta}$ within the FOV of the telescope and also assumes that the aberrations in the telescope are negligible for imaging between each deformable mirror and its conjugate plane.

Substituting Eq. (3.15) into Eq. (2.13) yields the computational formula

$$\begin{aligned} R_{ij} &= [Pr_i, Pr_j] \\ &= \int \mathrm{d}\boldsymbol{\theta} W_F(\boldsymbol{\theta}) \int \mathrm{d}\mathbf{x} W_A(\mathbf{x}) \\ &\quad \times \left[h_i(\mathbf{x} + d_i\boldsymbol{\theta}) - \sum_k f_k(\mathbf{x}) \int \mathrm{d}\mathbf{x}' W_A(\mathbf{x}') f_k(\mathbf{x}') \right. \\ &\quad \left. \times\, h_i(\mathbf{x}' + d_i\boldsymbol{\theta}) \right] \\ &\quad \times \left[h_i(\mathbf{x} + d_i\boldsymbol{\theta}) - \sum_k f_k(\mathbf{x}) \int \mathrm{d}\mathbf{x}' W_A(\mathbf{x}') f_k(\mathbf{x}') \right. \\ &\quad \left. \times\, h_i(\mathbf{x}' + d_i\boldsymbol{\theta}) \right], \end{aligned} \tag{3.16}$$

for the actuator cross-coupling matrix R. Removing the piston mode and possibly the tilt modes from the optical actuator influence function $r_i(\mathbf{x}, \boldsymbol{\theta})$ independently in each direction $\boldsymbol{\theta}$ in the FOV of the telescope is not equivalent to removing the same modes from the physical influence function $h_i(\mathbf{x})$.

The matrix coefficient G_{ji} that describes the first-order coupling between the deformable-mirror actuator i and the guide-star measurement j is a function of the actuator influence function $h_i(\mathbf{x})$ and of the range and the direction of the guide star. Combining Eqs. (3.6) and (3.8) and substituting the influence function $h_i(\mathbf{x})$ for the refractive-index layer $n(\mathbf{x}, d_i)$ gives

$$G_{ij} = \frac{2\pi}{\lambda} \int \mathrm{d}\mathbf{x} W_j^s(\mathbf{x}) h_i\left[\mathbf{x} + \left(\frac{d_i}{z_j}\right)(\mathbf{p}^j - \mathbf{x})\right]. \tag{3.17}$$

C. Covariance Calculations

We must also compute the covariance matrices A and S and the open-loop mean-square phase error $\langle\epsilon_0{}^2\rangle$ to evaluate adaptive-optics system performance with the expressions that are derived in Section 2. Using Eqs. (2.4), (2.24)–(2.26), and (3.15), we describe these quantities by

$$\begin{aligned} \langle\epsilon_0{}^2\rangle &= \langle[P\phi, P\phi]\rangle \\ &= \int \mathrm{d}\boldsymbol{\theta} W_F(\boldsymbol{\theta}) \int \mathrm{d}\mathbf{x} W_A(\mathbf{x}) \langle[\tilde{\phi}(\mathbf{x}, \boldsymbol{\theta}, t)]^2\rangle, \end{aligned} \tag{3.18}$$

$$\begin{aligned} A_{ij} &= \langle[P\phi, Pr_i] s_j(t)\rangle \\ &= \int \mathrm{d}\boldsymbol{\theta} W_F(\boldsymbol{\theta}) \int \mathrm{d}\mathbf{x} W_A(\mathbf{x}) \langle\tilde{\phi}(\mathbf{x}, \boldsymbol{\theta}, t) s_j(t)\rangle \\ &\quad \times \left[h_i(\mathbf{x} + \mathrm{d}_i\boldsymbol{\theta}) - \sum_k f_k(\mathbf{x}) \int \mathrm{d}\mathbf{x}' W_A(\mathbf{x}') f_k(\mathbf{x}') \right. \\ &\quad \left. \times\, h_i(\mathbf{x}' + d_i\boldsymbol{\theta}) \right], \end{aligned} \tag{3.19}$$

$$S_{ij} = \langle s_i(t) s_j(t)\rangle. \tag{3.20}$$

We now develop evaluation formulas for these quantities, using our geometric-optics models for the phase-distortion profile $\tilde{\phi}(\mathbf{x}, \boldsymbol{\theta}, t)$ and the wave-front slope sensor measurement vector $\mathbf{s}(t)$.

The three statistical terms that are to be evaluated in Eqs. (3.18)–(3.20) are of the form $\langle u_i u_j\rangle$, where u_i and u_j are either wave-front slope sensor measurements or values of turbulence-induced phase-distortion profiles. The common integral representation that is given by Eq. (3.9) for both quantities provides the starting point for evaluating this covariance:

$$\begin{aligned} \langle u_i u_j\rangle &= \left(\frac{2\pi}{\lambda}\right)^2 \iint \mathrm{d}\mathbf{x}_1 \mathrm{d}\mathbf{x}_2 v_i(\mathbf{x}_1) v_j(\mathbf{x}_2) \\ &\quad \times \int_0^\infty \int_0^\infty \mathrm{d}\tau_1 \mathrm{d}\tau_2 w_i(\tau_1) w_j(\tau_2) \\ &\quad \times \int_0^{z_i} \int_0^{z_j} \mathrm{d}\zeta_1 \mathrm{d}\zeta_2 \left\langle n\left[\mathbf{x}_1 + \left(\frac{\zeta_1}{z_i}\right), \zeta_1, t - \tau_1\right] \right. \\ &\quad \left. \times\, n\left[\mathbf{x}_2 + \left(\frac{\zeta_2}{z_j}\right), \zeta_2, t - \tau_2\right] \right\rangle \\ &\quad + \int_0^\infty \int_0^\infty \mathrm{d}\tau_1 \mathrm{d}\tau_2 w_i(\tau_1) w_j(\tau_2) \langle\alpha_i(t - \tau_1) \alpha_j(t - \tau_2)\rangle. \end{aligned} \tag{3.21}$$

The first step in reducing this expression utilizes the Taylor hypothesis [Eq. (3.3)], the Kolmogorov spectrum for refractive-index fluctuations [Eq. (3.4)], and the statistics of wave-front-sensor measurement noise [Eq. (3.7)] to yield the result

$$\begin{aligned}\langle u_i u_j\rangle = 9.69 \times 10^{-3}\left(\frac{2\pi}{\lambda}\right)^2 \iint \mathrm{d}\mathbf{x}_1 \mathrm{d}\mathbf{x}_2 v_i(\mathbf{x}_1) v_j(\mathbf{x}_2)\\ \times \int_0^\infty \int_0^\infty \mathrm{d}\tau_1 \mathrm{d}\tau_2 w_i(\tau_1) w_j(\tau_2) \int_0^{\min(z_i, z_j)} \mathrm{d}\zeta C_n^2(\zeta)\\ \times \left\{ \int \mathrm{d}\boldsymbol{\kappa}\kappa^{-11/3} \exp(-2\pi i \boldsymbol{\kappa}\cdot\boldsymbol{\Delta}) \right.\\ \left. \times \langle \exp[-2\pi i(\tau_1 - \tau_2)\boldsymbol{\kappa}\cdot\mathbf{v}]\rangle + c\right\}\\ + \delta_{ij} P_i \int_0^\infty \mathrm{d}\tau w_i^2(\tau).\end{aligned} \tag{3.22}$$

The integral with respect to $\boldsymbol{\kappa}$ is performed over the spatial-frequency domain, and the vector $\boldsymbol{\Delta}$ is defined by

$$\boldsymbol{\Delta} = \mathbf{x}_1 - \mathbf{x}_2 + \left(\frac{\zeta}{z_i}\right)(\mathbf{p}^i - \mathbf{x}_1) - \left(\frac{\zeta}{z_j}\right)(\mathbf{p}^j - \mathbf{x}_2). \tag{3.23}$$

$\boldsymbol{\Delta}$ is analogous to the quantities $\boldsymbol{\Delta}p_{oo}$, $\boldsymbol{\Delta}p_{og}$, and $\boldsymbol{\Delta}p_{gg}$ that appear in previous research.[7] The remaining expected-value operation that appears in Eq. (3.22) averages over the uniformly distributed direction of the wind-velocity vector $\mathbf{v}$. Note that an as-yet unspecified additive constant c has been introduced within the altitude integration in Eq. (3.22). As a result of Eq. (3.14) this constant may take any value that is independent of $\mathbf{x}_1$ and $\mathbf{x}_2$ without altering the value of the overall expression.

The remaining expected value that appears in Eq. (3.22) can be evaluated in terms of the Bessel function $J_0(z)$ with Eq. (9.1.21) of Olver[25] and the assumption of a uniformly distributed wind direction. The integral with respect to the angular component of $\boldsymbol{\kappa}$ may be similarly evaluated, and Eq. (3.22) can be further simplified by the change of integration variable defined by $\delta = (\tau_1 - \tau_2)$, $\tau = (\tau_1 + \tau_2)/2$. The constant c may now be assigned the value

$$c = -9.69 \times 10^{-3} 2\pi \int_0^\infty \mathrm{d}\kappa\kappa^{-8/3} J_0(2\pi|\tau_1 - \tau_2|\kappa v) \tag{3.24}$$

to cancel the singularity in the κ integration. The combined result of these substitutions is

$$\begin{aligned}\langle u_i u_j\rangle = 2\pi\, 9.69 \times 10^{-3}\left(\frac{2\pi}{\lambda}\right)^2 \iint \mathrm{d}\mathbf{x}_1 \mathrm{d}\mathbf{x}_2 v_i(\mathbf{x}_1) v_j(\mathbf{x}_2)\\ \times \int_{-\infty}^\infty \mathrm{d}\delta\left[\int_0^\infty \mathrm{d}\tau w_i(\tau + \delta/2) w_j(\tau - \delta/2)\right]\\ \times \int_0^{\min(z_i, z_j)} \mathrm{d}\zeta C_n^2(\zeta) \int_0^\infty \mathrm{d}\kappa\kappa^{-8/3} J_0(2\pi\delta\kappa v)\\ \times [J_0(2\pi\kappa\Delta) - 1] + \delta_{ij} P_i \int_0^\infty \mathrm{d}\tau w_i^2(\tau).\end{aligned} \tag{3.25}$$

Statistical characterizations of atmospheric turbulence are frequently expressed in terms of the quantity $(D/r_0)^{5/3}$, where D is the diameter of the telescope aperture and r_0 is Fried's turbulence-induced effective-coherence diameter.[26] The covariance $\langle u_i u_j\rangle$ can be expressed in this form by the change of integration variable $\nu = \pi D\kappa$ and the identity

$$1 = r_0^{-5/3}\left[\frac{2.91}{6.88}\left(\frac{2\pi}{\lambda}\right)^2 \int_0^\infty \mathrm{d}\zeta C_n^2(\zeta)\right]^{-1}, \tag{3.26}$$

which is an algebraic rearrangement of the definition for r_0. The final expression for $\langle u_i u_j\rangle$ takes the form

$$\begin{aligned}\langle u_i u_j\rangle = 0.97\left(\frac{D}{r_0}\right)^{5/3}\left[\int_0^\infty \mathrm{d}\zeta C_n^2(\zeta)\right]^{-1} \iint \mathrm{d}\mathbf{x}_1 \mathrm{d}\mathbf{x}_2 v_i(\mathbf{x}_1) v_j(\mathbf{x}_2)\\ \times \int_{-\infty}^\infty \mathrm{d}\delta\left[\int_0^\infty \mathrm{d}\tau w_i(\tau + \delta/2) w_j(\tau - \delta/2)\right]\\ \times \int_0^{\min(z_i, z_j)} \mathrm{d}\zeta C_n^2(\zeta) f\left(\frac{2\delta v}{D}, \frac{2\Delta}{D}\right) + \delta_{ij} P_i \int_0^\infty \mathrm{d}\tau w_i^2(\tau),\end{aligned} \tag{3.27}$$

where the function $f(a, b)$ is an abbreviation for the integral

$$f(a, b) = \int_0^\infty \mathrm{d}\nu\nu^{-8/3} J_0(a\nu)[J_0(b\nu) - 1]. \tag{3.28}$$

Equations (3.18)–(3.20), (3.23), (3.27), and (3.28) were used to compute the statistical quantities A, S, and $\langle\epsilon_0^2\rangle$ for the numerical results that are presented in Section 4. Appendix B evaluates the integral $f(a, b)$ in terms of a hypergeometric series, and Appendix C summarizes our approach to evaluating numerically the spatial and the temporal integrals that appear in Eqs. (3.18)–(3.20) and (3.27). Depending on the total number of subapertures and actuators, a few seconds to a few hours of CPU time on a high-performance workstation are necessary for numerical evaluation of the performance of an adaptive-optics system with these equations.

4. SAMPLE NUMERICAL RESULTS

This section contains numerical results describing the predicted performance of adaptive-optics systems of varying levels of complexity. Subsection 4.A revisits the subjects of fitting error and noise gain that have been considered previously by a variety of investigators.[11-15,24] These results incorporate the effects of circular apertures and partial wave-front-sensor subapertures at the edge of the pupil, two practical factors generally neglected in previous research. The aperture geometries that are evaluated include 25 to 393 actuators and 16 to 344 wave-front-sensor subapertures arranged in either the so-called Fried (common-subaperture) or Hudgin (displaced-subaperture) geometry.

Subsections 4.B–4.D describe the performance of sample adaptive-optics systems incorporating a single deformable mirror and single guide star, a single deformable mirror and multiple guide stars, and multiple deformable mirrors and multiple guide stars. We have not attempted to fit these results to simplified scaling laws because of the number of parameters that are necessary to describe the more complex adaptive-optics configurations. All the cases that we consider assume either a 3- or a 4-m telescope-aperture diameter, a 0.5-μm wavelength for performance evaluation, and the atmospheric turbulence

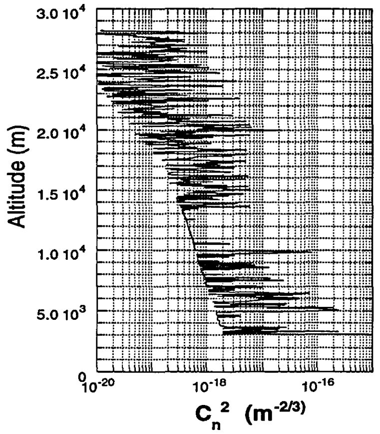

Fig. 3. Sample atmospheric turbulence $C_n^2(h)$ profile. This profile is derived from U.S. Air Force Geophysics Laboratory thermosonde data recorded on December 11, 1985. Integrating this profile yields the parameters $r_0 = 0.285$ m and $\theta_0 = 18.6$ μrad for a wavelength of 0.5 μm and a zenith angle of 0°.

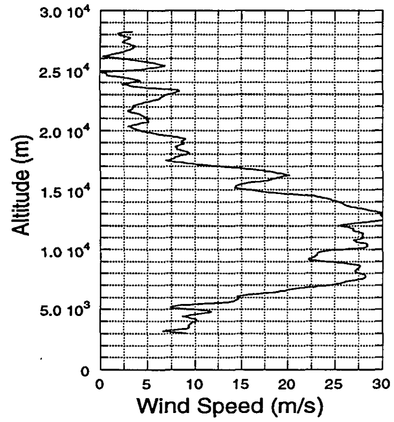

Fig. 4. Atmospheric-wind-speed profile. This profile was recorded simultaneously with Fig. 3. The associated Greenwood frequency is 19.7 Hz at $\lambda = 0.5$ μm.

$C_n^2(h)$ and wind-velocity profiles that are illustrated in Figs. 3 and 4. These profiles are an example of good seeing conditions that were recorded at Mt. Haleakala, Hawaii, by a U.S. Air Force Geophysics Laboratory thermosonde on December 11, 1985.[27] Integrating these profiles yields the parameter values $r_0 = 0.285$ m, $\theta_0 = 18.6$ μrad, and $f_g = 19.7$ Hz at a 0.5-μm wavelength and a zenith angle of 0°. Although seeing conditions that are this good are unusual at 0.5 μm, values that are this large for a wavelength of 1.0 μm were frequently recorded during the Air Force Geophysics Laboratory measurement program.

Adaptive-optics system performance is quantified in terms of mean-square residual phase error, expected long- and short-exposure OTF's, and long- and short-exposure Strehl ratios. Mean-square phase errors were computed with Eq. (2.23). Expected long- and short-exposure OTF's were computed with the expression

$$\mathrm{OTF}(\boldsymbol{\kappa}, \boldsymbol{\theta}) = \frac{\int \mathrm{d}\mathbf{x} W_A(\mathbf{x}) W_A(\mathbf{x} - \lambda\boldsymbol{\kappa}) \exp[-\tfrac{1}{2} D(\mathbf{x}, \mathbf{x} - \lambda\boldsymbol{\kappa}, \boldsymbol{\theta})]}{\int \mathrm{d}\mathbf{x} W_A{}^2(\mathbf{x})}, \quad (4.1)$$

where $D(\mathbf{x}, \mathbf{x}', \boldsymbol{\theta}) = \langle[\epsilon(\mathbf{x}, \boldsymbol{\theta}) - \epsilon(\mathbf{x}', \boldsymbol{\theta})]^2\rangle$ is the structure function of the residual-phase-distortion profile ϵ in the direction $\boldsymbol{\theta}$. This expression describes either long- or short-exposure OTF's according to whether only the piston mode or both the piston and the tilt modes have been removed from the phase profile $\epsilon(\mathbf{x}, \boldsymbol{\theta})$. The structure function $D(\mathbf{x}, \mathbf{x}', \boldsymbol{\theta})$ is related to the second-order statistics of ϵ by the identity

$$D(\mathbf{x}, \mathbf{x}', \boldsymbol{\theta}) = \langle\epsilon^2(\mathbf{x}, \boldsymbol{\theta})\rangle + \langle\epsilon^2(\mathbf{x}', \boldsymbol{\theta})\rangle - 2\langle\epsilon(\mathbf{x}, \boldsymbol{\theta})\epsilon(\mathbf{x}', \boldsymbol{\theta})\rangle, \quad (4.2)$$

and the three terms on the right-hand side of this equation can be computed with the formula

$$\begin{aligned}
\langle\epsilon(\mathbf{x}, \boldsymbol{\theta})\epsilon(\mathbf{x}', \boldsymbol{\theta})\rangle
&= \left\langle\left[\tilde{\phi}(\mathbf{x}, \boldsymbol{\theta}) - \sum_i \tilde{r}_i(\mathbf{x}, \boldsymbol{\theta}) \sum_j M_{ij} s_j\right] \times \left[\tilde{\phi}(\mathbf{x}', \boldsymbol{\theta}) - \sum_{i'} \tilde{r}_{i'}(\mathbf{x}', \boldsymbol{\theta}) \sum_{j'} M_{i'j'} s_{j'}\right]\right\rangle \\
&= \langle\tilde{\phi}(\mathbf{x}, \boldsymbol{\theta})\tilde{\phi}(\mathbf{x}', \boldsymbol{\theta})\rangle - \sum_{i'} \tilde{r}_{i'}(\mathbf{x}', \boldsymbol{\theta}) \sum_{j'} M_{i'j'} \langle\tilde{\phi}(\mathbf{x}, \boldsymbol{\theta}) s_{j'}\rangle \\
&\quad - \sum_i \tilde{r}_i(\mathbf{x}, \boldsymbol{\theta}) \sum_j M_{ij} \langle\tilde{\phi}(\mathbf{x}', \boldsymbol{\theta}) s_j\rangle \\
&\quad + \sum_{ii'} \tilde{r}_i(\mathbf{x}, \boldsymbol{\theta}) \tilde{r}_{i'}(\mathbf{x}', \boldsymbol{\theta}) \sum_{jj'} M_{ij} M_{i'j'} \langle s_j s_{j'}\rangle. \quad (4.3)
\end{aligned}$$

The covariance terms appearing in Eq. (4.3) may be evaluated with Eq. (3.27) from Subsection 3.C. Finally, long- or short-exposure Strehl ratios are computed by integration of the corresponding OTF.

A. Fitting Error and Noise Gain

We can evaluate the wave-front fitting error for a given adaptive-optics actuator–subaperture configuration by applying the techniques that are developed here to a sample problem with zero wind velocity, a single ground-level turbulence layer, and a noise-free wave-front slope sensor. As a result of Eq. (3.27), the mean-square residual phase variance is proportional to the quantity $(D/r_0)^{5/3}$ in this special case. The constant of proportionality depends on the system's actuator–subaperture geometry and the deformable-mirror actuator influence function. The right-hand asymptotes of Figs. 2 and 5 of Wallner[12] suggest that the mean-square fitting error is accurately approximated by a scaling law of the form

$$\langle\epsilon^2\rangle = c_F(L/r_0)^{5/3}, \quad (4.4)$$

where c_F is the so-called fitting-error coefficient and L is the width of a wave-front-sensor subaperture. Further details of the subaperture and actuator geometries evidently have little bearing on the value of the fitting error, at least for square apertures containing 1 to 36 subapertures in either the common-subaperture or the displaced-subaperture configuration. The first results of this section investigate this hypothesis for larger, circular, apertures and compare the fitting error for minimal-variance estimators with and without closed-loop constraints.

Fitting-error coefficients have been computed for the Fried and Hudgin subaperture geometries with $D/L = 4$, 8, 12, 16, 20. The two subaperture geometries that

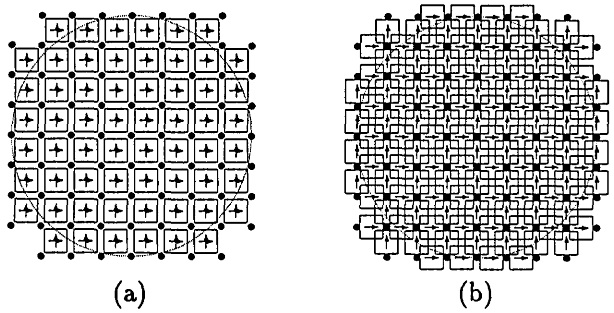

Fig. 5. Actuator–subaperture geometries evaluated for fitting-error coefficients. This figure illustrates (a) the Fried and (b) the Hudgin actuator–subaperture geometries with eight subapertures/aperture diameter. The large open circles represent the telescope aperture, and the actuator locations are indicated by the dots. Wave-front-sensor subapertures and the gradient components that are measured are indicated by the small squares and vectors. The edge subapertures are truncated by the boundary of the telescope aperture. The small gaps between the subapertures appear only for purposes of illustration.

were evaluated with $D/L = 8$ are illustrated in Fig. 5. Partial wave-front-sensor subapertures and deformable-mirror actuators that are located outside but coupling into the clear aperture were included in the analysis. The results that were obtained also assume a linear-spline actuator influence function. As described in Appendix C, the necessary spatial integrals were evaluated with Simpson's rule on a grid of points with $2D/L$ points/aperture diameter.

Figure 6 plots the fitting-error results that were obtained for the constrained and unconstrained minimal-variance estimators and the Fried and the Hudgin subaperture geometries. For $D/L \geq 12$, these results can be approximated by the scaling laws

$$\langle \epsilon^2 \rangle/(L/r_0)^{5/3} = \begin{cases} 0.305 & \text{(unconstrained estimator, Fried geometry)} \\ 0.325 & \text{(constrained estimator, Fried geometry)} \\ 0.350 & \text{(unconstrained estimator, Hudgin geometry)} \\ 0.365 & \text{(constrained estimator, Hudgin geometry)} \end{cases}. \tag{4.5}$$

The performance penalty associated with closed-loop constraints is no more than a factor of 7% in mean-square phase error, which is significantly smaller than the factor of 30% indicated by the right-hand asymptotes of Fig. 3 of Wallner.[12] This difference is attributable to the fact that Wallner's closed-loop estimator is the noise-optimal least-squares estimator that is evaluated under conditions of zero measurement noise. The performance variation between the two subaperture geometries is typically between 10% and 15%. The remaining results in this section are for the case of the Fried geometry.

To parameterize the combined effect of the fitting error and the wave-front-sensor noise on the reconstructor performance, it is useful to rewrite Eq. (3.27) in the form

$$\begin{aligned} \frac{\langle u_i u_j \rangle}{(L/r_0)^{5/3}} &= 0.97\left(\frac{D}{L}\right)^{5/3}\left[\int_0^\infty \mathrm{d}\zeta C_n^2(\zeta)\right]^{-1} \\ &\times \iint \mathrm{d}\mathbf{x}_1 \mathrm{d}\mathbf{x}_2 v_i(\mathbf{x}_1) v_j(\mathbf{x}_2) \\ &\times \int_{-\infty}^{\infty} \mathrm{d}\delta \left[\int_0^\infty \mathrm{d}\tau w_i(\tau + \delta/2) w_j(\tau - \delta/2)\right] \\ &\times \int_0^{\min(z_i, z_j)} \mathrm{d}\zeta C_n^2(\zeta) f\left(\frac{2\delta v}{D}, \frac{2\Delta}{D}\right) \\ &+ \delta_{ij} P_i \int_0^\infty \mathrm{d}\tau w_i^2(\tau)/(L/r_0)^{5/3}. \end{aligned} \tag{4.6}$$

All the covariances $\langle u_i u_j \rangle$ that determine the residual mean-square phase error for the reconstructor are proportional to $(L/r_0)^{5/3}$. The constant of proportionality depends on the actuator–subaperture geometry of the adaptive-optics system and on the term $P_i \int_0^\infty \mathrm{d}\tau w_i^2(\tau)/(L/r_0)^{5/3}$. The latter quantity may be interpreted as the mean-square wave-front-sensor noise level that first is scaled by the noise gain of the adaptive-optics servo filter and then is normalized by the relative level of turbulence within an individual wave-front-sensor subaperture.

Figures 7 and 8 plot the tilt-included and the tilt-removed mean-square wave-front reconstruction errors, respectively, as a function of D/L and the normalized rms wave-front-sensor noise level. These results assume that

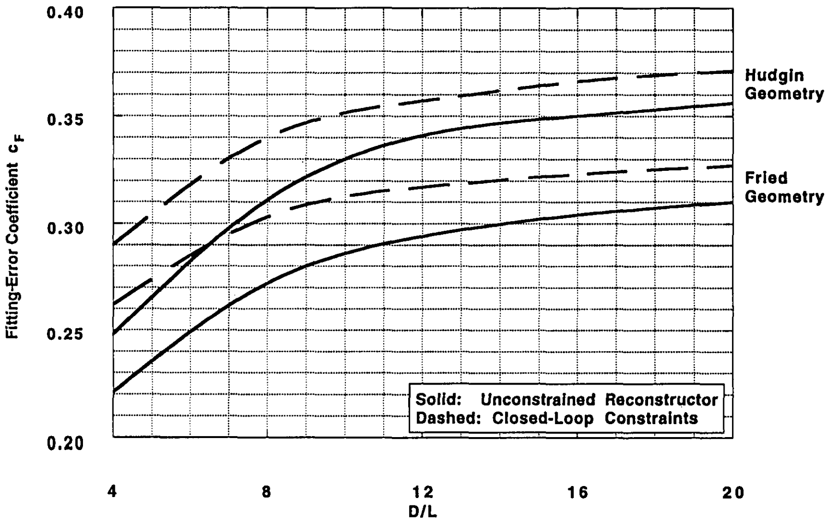

Fig. 6. Fitting-error results for minimal-variance reconstructors with and without closed-loop constraints. Here D is the telescope-aperture diameter, L is the width of a subaperture, and the mean-square phase error resulting from fitting error is $c_F(D/r_0)^{5/3}$.

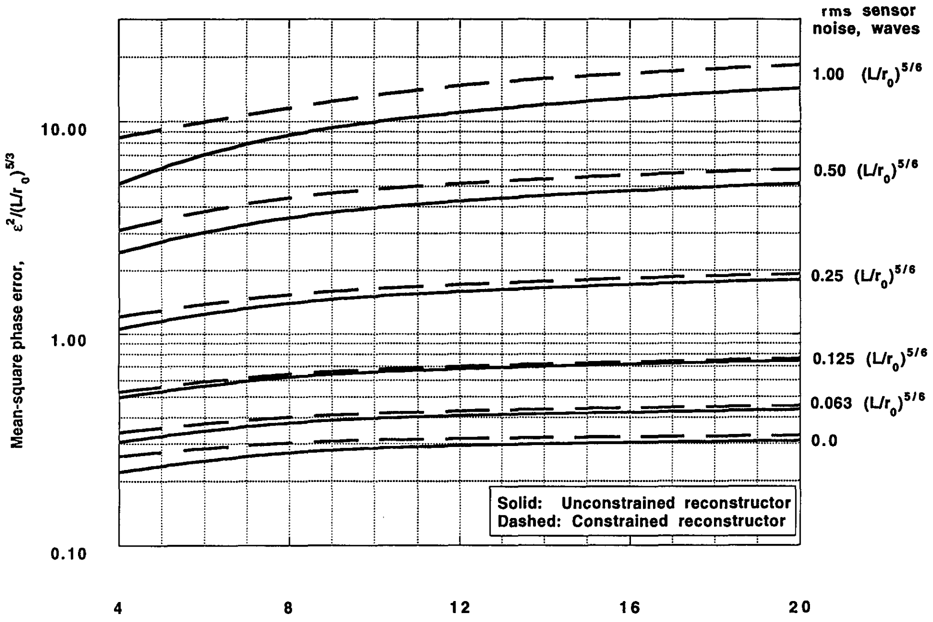

Fig. 7. Mean-square tilt-included wave-front reconstruction error versus D/L and wave-front-sensor noise level. Here D is the telescope-aperture diameter, L is the width of a subaperture, the sensor noise is expressed in terms of rms waves of phase-difference measurement accuracy, and ϵ^2 is the mean-square residual phase error resulting from both noise and fitting error.

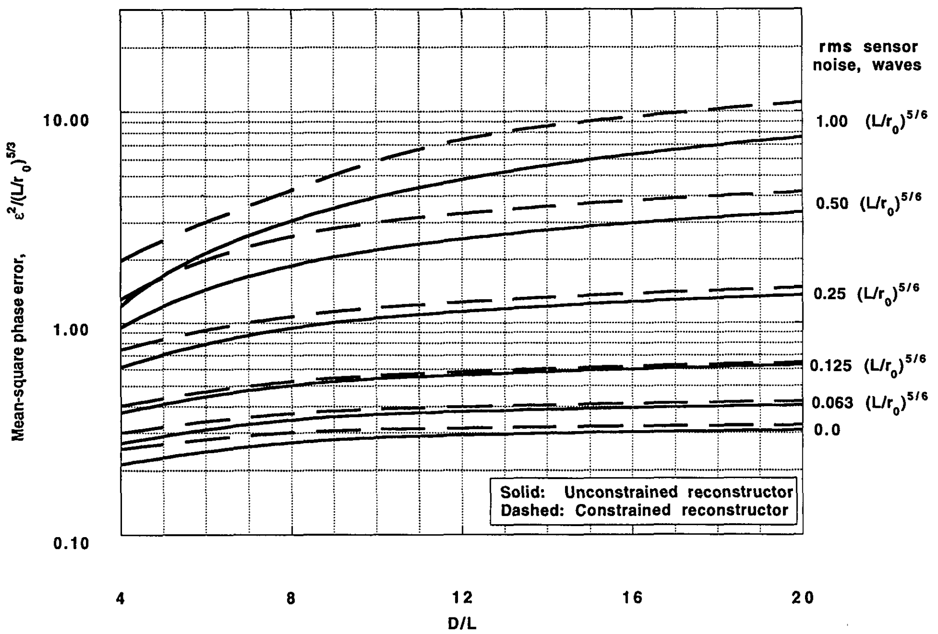

Fig. 8. Mean-square tilt-removed wave-front reconstruction error versus D/L and wave-front-sensor noise level. This figure is identical to Fig. 7, except that full-aperture wave-front tilt is not included in calculating the phase variance ϵ^2.

the mean-square wave-front slope measurement error on partial subapertures is inversely proportional to the subaperture area. For $D/L \geq 8$ and rms wave-front-sensor noise levels that are no greater than $0.25(L/r_0)^{5/6}$, the performance penalty that is associated with the closed-loop reconstructor is no greater than 10% in wave-front variance. This penalty increases for larger noise levels, but not until the mean-square error for both reconstructors is approximately an order of magnitude greater than the no-noise limit imposed by the fitting error. Unlike what is shown in Fig. 3 of Wallner,[12] the performance of the closed-loop reconstructor never diverges dramatically from the open-loop case. As the sensor noise level increases, the range space of the closed-loop minimum-variance reconstructor is reduced to include only those wave-front modes for which the expected magnitude of turbulence is greater than the expected estimation error resulting from measurement noise.

The effect of sensor noise on wave-front reconstruction accuracy is frequently estimated by use of a formula of the form[13–15]

$$\sigma_N{}^2 = (C_1 + C_2 \ln N_S)\sigma_{PD}{}^2, \tag{4.7}$$

where $\sigma_N{}^2$ is the mean-square phase-estimation error that

Table 1. Short-Exposure Strehl Ratio versus Control-Loop Bandwidth (f) and Sensor Noise Level at $\lambda = 0.5\ \mu$m for a 4-m-Aperture Telescope with 0.25-m Subapertures under the Atmospheric Conditions Given in Figs. 3 and 4

	$f =$			
Noise at $10f$, Waves	∞	30 Hz	20 Hz	10 Hz
Natural guide star				
0.00	0.772	0.647	0.549	0.312
0.05		0.632	0.537	0.306
0.10		0.604	0.513	0.294
0.20		0.514	0.438	0.253
Sodium guide star (z = 90 km)				
0.00	0.598	0.517	0.445	0.263
0.05		0.503	0.433	0.256
0.10		0.481	0.414	0.246
0.20		0.411	0.355	0.213
Rayleigh-backscatter guide star (z = 20 km)				
0.00	0.141	0.138	0.129	0.096
0.05		0.131	0.123	0.091
0.10		0.126	0.118	0.088
0.20		0.112	0.105	0.079

is due to noise, σ_{PD}^2 is the mean-square phase-difference measurement error for a single wave-front-sensor measurement, N_S is the total number of wave-front-sensor subapertures, and C_1 and C_2 are coefficients depending on the wave-front reconstruction algorithm and the wave-front-sensor geometry. The values $C_1 = 0.239$ and $C_2 = 0.101$ yield a good fit to the results that are plotted in Fig. 7 for the smaller noise levels.

B. Single Guide-Star Results

This subsection contains numerical results describing the performance of three different guide-star options for a 4-m telescope imaging at a 0.5-μm wavelength under the good seeing conditions that are presented in Figs. 3 and 4. The three guide-star options that are considered are a natural on-axis guide star, a mesospheric sodium-layer guide star at a 90-km altitude, and a guide-star generated with Rayleigh backscatter from an altitude of 20 km. For this sample problem we chose a subaperture width of 0.25 m, which approximately matches the r_0 value of 0.285 m for the $C_n^2(z)$ profile in Fig. 3. The guide-star options are evaluated in terms of their short-exposure Strehl ratios and OTF's for a variety of different control-loop bandwidths and wave-front-sensor noise levels. Results on long-exposure performance are deferred until Subsection 4.C, which discusses multiple-guide-star systems, since a single laser guide star cannot be used to measure overall wave-front tilt.

Table 1 lists the short-exposure Strehl ratios for the three guide-star choices over a range of bandwidths and noise levels. The finite servo bandwidths of 10, 20, and 30 Hz bracket the 19.6-Hz Greenwood frequency for the wind profile in Fig. 4. The noise levels that are listed in Table 1 are specified at a wave-front-sensor sampling rate that is assumed to be a factor of 10 larger than the control-loop bandwidth. The corresponding noise levels at the control-loop bandwidth will be attenuated by a factor of $(\pi/10)^{1/2} = 0.56$. The short-exposure Strehl ratio for the natural guide star with zero noise and infinite bandwidth reflects the effect of the fitting error for the common-subaperture geometry and the parameter values $D/L = 16$ and $L/r_0 = 0.25/0.285 = 0.877$. The noise-free, infinite-bandwidth Strehl ratios for the two laser-guide-star options incorporate the additional wave-front reconstruction error resulting from focus anisoplanatism. This is a relatively modest effect for the mesospheric-sodium-layer guide star and a much more significant degradation for the Rayleigh-backscatter beacon at an altitude of 20 km. The Strehl ratios that were computed for finite control-loop bandwidths are significantly larger than what would be expected based on the standard scaling laws for long-exposure Strehl ratios[17,28] that neglect interactions with the fitting error and with focus anisoplanatism.

The degree of interaction between wave-front-sensor noise and other error sources can be estimated from a comparison of Table 1 and Fig. 8. For example, a wave-front-sensor noise level of 0.1 wave at the wave-front-sensor sampling rate corresponds to a normalized noise level of $[0.1 \times 0.56/0.877^{5/6}] \times (L/r_0)^{5/6} = 0.0625(L/r_0)^{5/6}$ wave at the control-loop bandwidth. Using Fig. 8, we find that the predicted increase in the mean-square phase error that is due to this noise level with $D/L = 16$ equals $0.097(L/r_0)^{5/3} = 0.078$, which corresponds to a relative Strehl-ratio reduction of approximately $\exp(-0.078) = 0.925$. The Strehl ratios that are listed in Table 1 for the 0.1-wave noise level, which account for the interactions between noise and other error sources, are degraded by a factor in the range of 0.912–0.937 from the Strehl ratios that are computed for 0.0-wave measurement noise. The corresponding Strehl-ratio losses for a 0.2-wave noise level at the sensor sampling rate are 0.788 (Fig. 8) and 0.791–0.831 (Table 1). The Strehl-ratio degradation that is due to wave-front-sensor noise is effectively decoupled from focus anisoplanatism and servo-bandwidth effects for the representative noise and bandwidth parameters that are given in Table 1.

Short-exposure OTF's corresponding to the Strehl ratios that are listed in Table 1 are presented in Figs. 9–12. The results for the zero-sensor-noise, infinite control-loop bandwidth case are plotted in Fig. 9. The OTF's for either the natural guide star or the mesospheric-sodium-layer guide star are proportional to the diffraction-limited OTF at all but the lowest spatial frequencies, with a constant of proportionality equal to the noise-free, infinite-bandwidth Strehl ratio that is listed in Table 1. The OTF for the Rayleigh-backscatter guide star at 20 km is not a scaled version of the diffraction-limited result but does remain within an order of magnitude of the diffraction-limited OTF at all spatial frequencies. All three cases represent an improvement of at least 2 orders of magnitude over the short-exposure OTF without adaptive optics.

Figures 10–12 plot the relative reduction to the short-exposure OTF's that are due to a finite control-loop bandwidth and a sensor noise level of 0.2 wave. With zero wave-front-sensor noise, the OTF reduction resulting from a loop bandwidth of 20 or 30 Hz for either the natural guide star or the mesospheric-sodium-layer guide star is constant to within 5% for all normalized spatial frequencies greater than 0.2. The OTF reduction at 10 Hz for these guide stars or at any bandwidth for the Rayleigh-

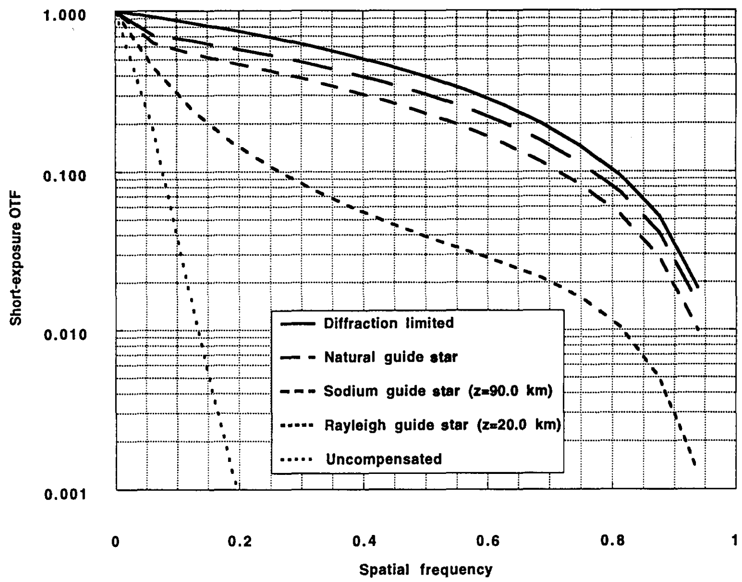

Fig. 9. Short-exposure OTF's resulting from anisoplanatism and fitting error at a 0.5-μm wavelength for $D = 4$ m, $L = 0.25$ m, $\psi = 0°$, and the atmospheric profiles shown in Figs. 3 and 4. These results assume zero wave-front-sensor measurement noise and an infinite wave-front control-loop bandwidth.

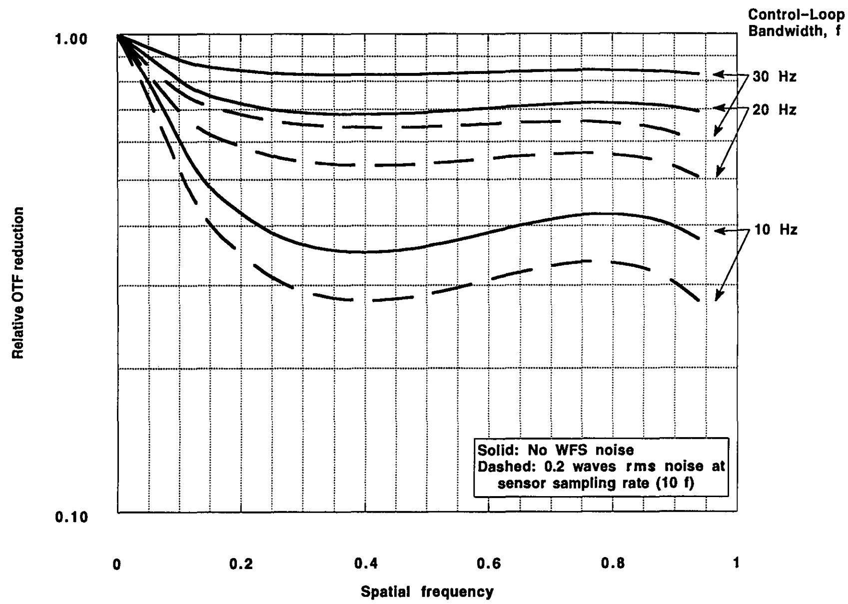

Fig. 10. Effect of noise and finite servo bandwidth on the short-exposure OTF for a natural on-axis guide star. These curves plot the ratios between short-exposure OTF's, including noise and finite-bandwidth effects and the noise-free, infinite-bandwidth OTF that is plotted in Fig. 9. Note that the wave-front-sensor (WFS) noise level is specified at a wave-front-sensor sampling rate that is ten times larger than the control-loop bandwidth.

backscatter guide star is more variable but differs by no more than ±20% for spatial frequencies between 0.2 and 0.9 times the diffraction-limited cutoff. The larger OTF variations for the Rayleigh-backscatter guide star indicate a stronger interaction between focus anisoplanatism and servo-bandwidth effects. Finally, the additional OTF reduction resulting from 0.2 wave of wave-front-sensor noise is approximately constant for all three guide stars and for servo bandwidths at spatial frequencies above 0.2 times the diffraction-limited cutoff.

C. Multiple-Guide-Star Results

The single-guide-star results that are presented above illustrate the relatively poor performance that is achievable with a single Rayleigh-backscatter guide star for large-aperture visible-wavelength adaptive optics. The number of stars that are sufficiently bright to serve as natural guide stars for visible imaging is very limited, however, and illuminator lasers that have sufficient power and beam quality to generate bright mesospheric-sodium-layer beacons have not yet been demonstrated. Guide-star constellations containing multiple beacons are one possible approach to obtaining improved OTF's and Strehl ratios with minimum reliance on natural or mesospheric-sodium-layer guide stars. Figure 13 plots the noise-free infinite-bandwidth short-exposure OTF's for three possible multiple-guide-star configurations. These results are for the same aperture diameter, atmospheric profiles, and

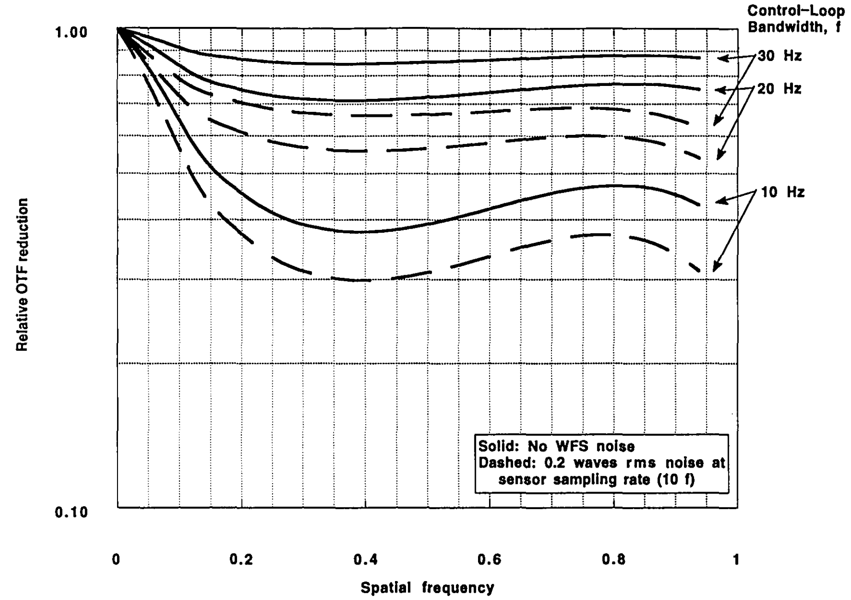

Fig. 11. Effect of noise and finite servo bandwidth on the short-exposure OTF for a resonant sodium guide star at $z = 90$ km. These curves assume a guide star in the mesospheric sodium layer but are otherwise similar to Fig. 10. WFS, wave-front sensor.

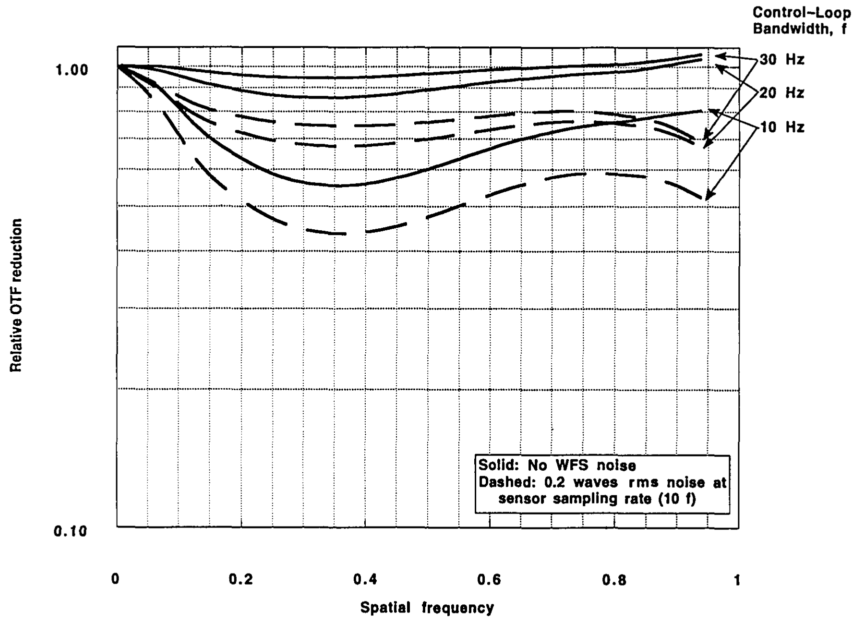

Fig. 12. Effect of noise and finite servo bandwidth on the short-exposure OTF for a Rayleigh-backscatter guide star at $z = 20$ km. These curves assume a guide-star altitude of 20 km but are otherwise similar to Fig. 11. WFS, wave-front sensor.

deformable-mirror actuator spacing as in Subsection 4.B. The guide-star constellations that are considered and the short-exposure Strehl ratios corresponding to the OTF's given in Fig. 13 are

- A constellation of four Rayleigh-backscatter guide stars at a 20-km altitude. The guide stars are transmitted with the full telescope aperture and arranged in a square with 2 m between guide stars. Each wave-front-sensor subaperture measures wave-front slopes for the guide star that is most nearly overhead. The short-exposure Strehl ratio for this option is 0.214.
- A constellation of one on-axis Rayleigh-backscatter guide star at a 20-km altitude and an on-axis mesospheric sodium-layer guide star. A separate wave-front sensor with four subapertures measures the wave-front slopes for the mesospheric sodium-layer guide star. The illuminator power that is necessary for the mesospheric sodium-layer beacon is greatly reduced from the single-beacon case because the subaperture area has increased by a factor of 64. The short-exposure Strehl ratio for this hybrid guide-star configuration is 0.260.
- A constellation of one on-axis Rayleigh-backscatter guide star at 20 km and an on-axis mesospheric sodium-layer guide star sensed with a wave-front sensor with 16 subapertures. The short-exposure Strehl ratio for this constellation is 0.433.

Guide-star position uncertainty significantly limits the OTF and the Strehl ratio that are achieved with four

Rayleigh guide stars. The Strehl ratio of 0.214 increases to 0.272 if this effect is neglected in the analysis. Results that are similar to those shown in Fig. 13 are achieved for larger-aperture telescopes with a hybrid guide-star constellation consisting of a bright mesospheric sodium-layer guide star and a dim natural guide star.

All laser-guide-star adaptive-optics systems are in some sense multiple-guide-star systems because a natural guide star must be used to sense full-aperture wave-front tilt. Natural guide stars that are sufficiently bright for this purpose have densities that are low relative to the size of the isoplanatic angle at visible wavelengths. Figures 14–16 illustrate how noise-free infinite-bandwidth long-exposure OTF's degrade because of the tilt anisoplanatism that is caused by angular displacement of the tracking guide star. These results are once again for a 4-m-aperture telescope, a 0.5-μm evaluation wavelength, a 0° zenith angle, a 0.25-m subaperture width, and the atmospheric turbulence and wind profiles that are given in Figs. 3 and 4. For Fig. 14 it is assumed that a single off-axis natural guide star is used for both tilt sensing and higher-order adaptive optics. In this case a guide-star separation of as little as 8 arcsec degrades the long-exposure OTF by an order of magnitude. Figures 15 and 16 plot results for a single on-axis laser guide star combined with an off-axis tracking guide star. Only wave-front tilt compensation is degraded by anisoplanatism for these curves, and the long-exposure OTF's that are

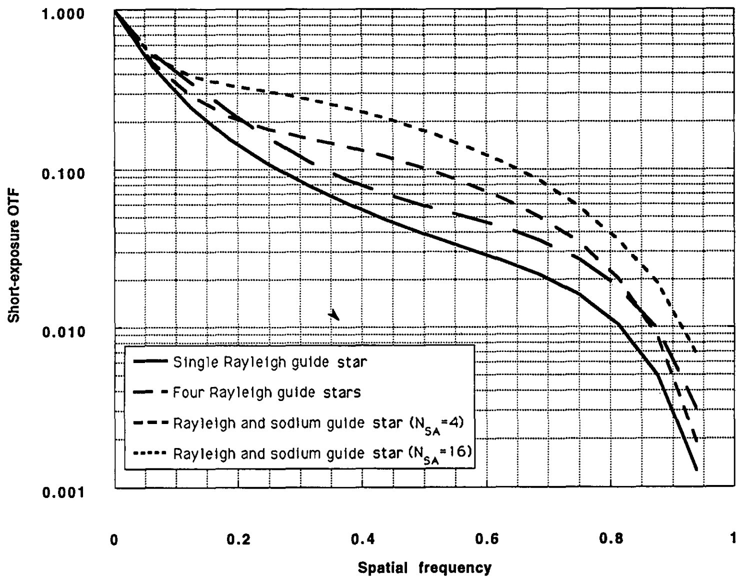

Fig. 13. Short-exposure OTF's resulting from anisoplanatism and fitting error for three multiple-guide-star constellations. These results are again for the parameter values $D = 4$ m, $L = 0.25$ m, $\psi = 0°$, and the atmospheric profiles shown in Figs. 3 and 4. These results also assume zero wave-front-sensor measurement noise and an infinite control-loop bandwidth. N_{SA} is the number of subapertures for the sodium-guide-star wave-front sensor. The Rayleigh-guide-star altitude is 20 km. Each guide star is sensed over a quadrant of the telescope aperture for the case of four Rayleigh guide stars.

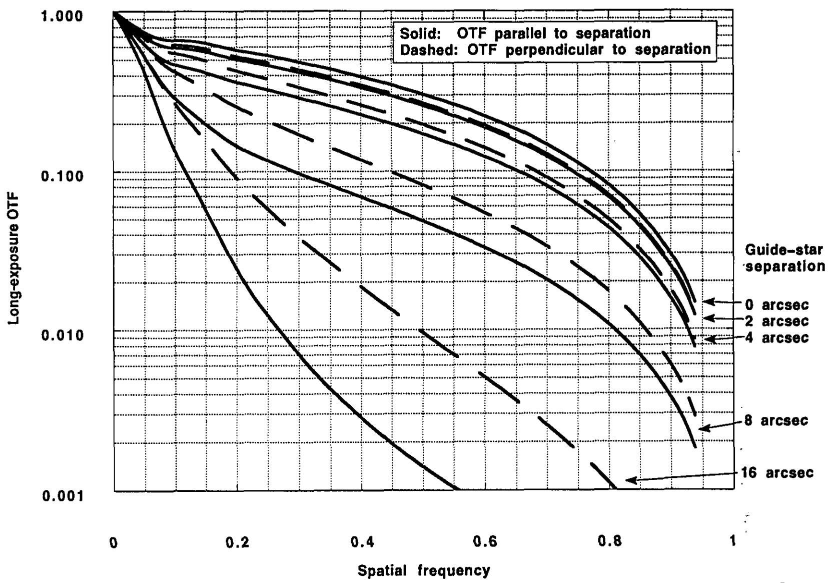

Fig. 14. Effect of guide-star offset on the long-exposure OTF for a single natural guide star. These results are again for the parameter values $D = 4$ m, $L = 0.25$ m, $\psi = 0°$, and the atmospheric profiles shown in Figs. 3 and 4. These results also assume zero wave-front-sensor measurement noise and an infinite control-loop bandwidth.

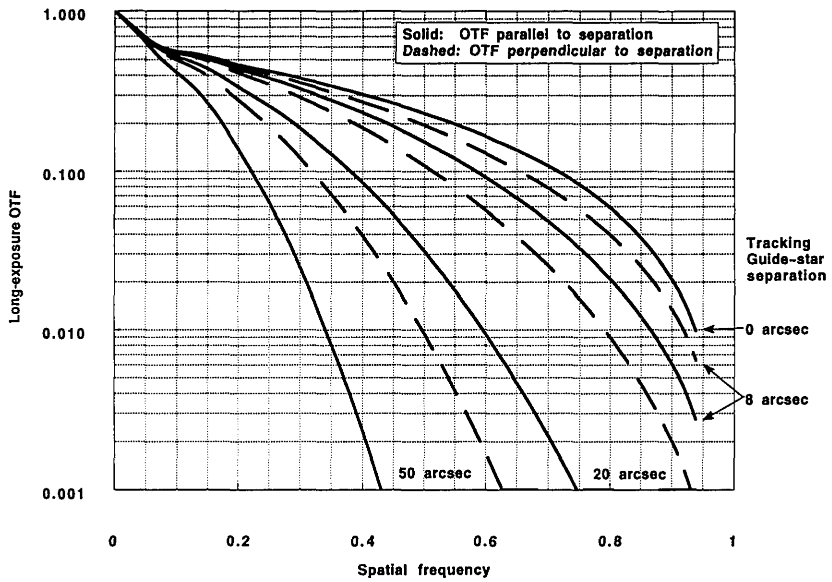

Fig. 15. Effect of tracking-guide-star offset on the long-exposure OTF for an on-axis resonant sodium guide star at $z = 90$ km. These curves are for the case of a mesospheric-sodium-layer guide star but are otherwise similar to Fig. 14.

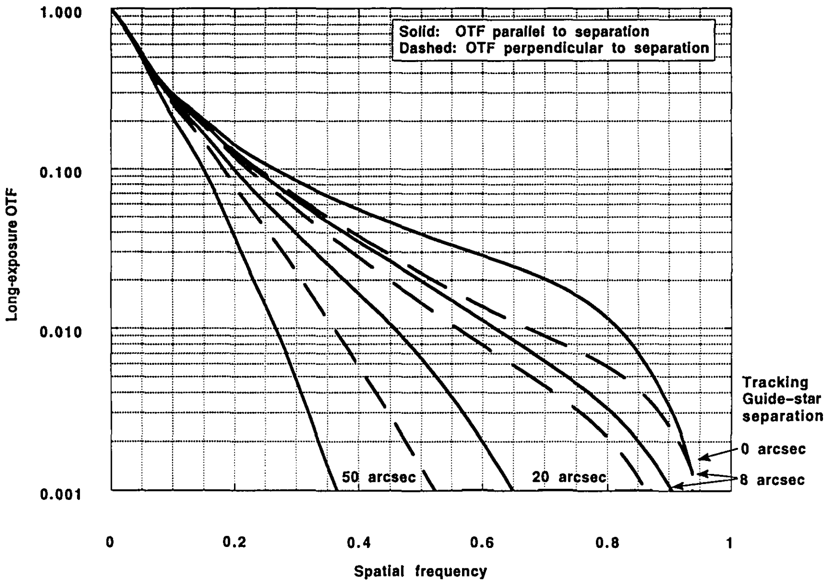

Fig. 16. Effect of tracking-guide-star offset on long-exposure OTF for an on-axis Rayleigh-backscatter guide star at $z = 20$ km. These curves are for the case of a 20-km guide-star altitude but are otherwise similar to Fig. 14.

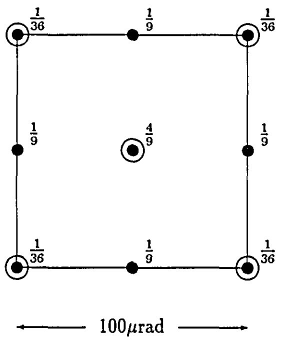

Fig. 17. FOV and guide-star geometries for multiconjugate adaptive-optics calculations. The telescope FOV that is to be compensated is a square that is 100 μrad in width. The five circles indicate the directions of natural and/or laser guide stars used for wave-front sensing. The wave-front reconstruction algorithm is selected to minimize the weighted sum of residual mean-square phase errors at nine points in the FOV, as indicated by the points and the weights.

achieved with an on-axis laser guide star and a displaced tracking guide star are significantly larger than the OTF for a single natural guide star that is displaced by a comparable angle.

Complete sky coverage at visible wavelengths with laser-guide-star adaptive optics will require either accurate tracking with very dim guide stars or guide-star offsets that are considerably larger than 20 arcsec. For example, the density of $m \leq 17.3$ stars that provide a flux of at least 1100 (photons/m^2)/s in the 0.55 ± 0.09 μm spectral band is ~0.25 star per square arcmin outside the plane of the galaxy.[29] Practical techniques for accurate tilt-anisoplanatism compensation with large guide-star offsets have not yet been identified.

D. Multiconjugate Results

The parameter space of possible multiconjugate adaptive-optics configurations is so large that we did not attempt to develop scaling laws that characterize the performance of an extended range of potential systems. Instead we focused attention on one particular implementation to quantify the potential performance advantage of multiconjugate adaptive optics in at least one special case. Figure 17 illustrates the FOV and guide-star geometries that are assumed for these sample calculations. The FOV is a square of width 100 μrad (20.6 arcsec). The FOV weighting function $W_F(\boldsymbol{\theta})$ is a linear combination of nine delta functions located at the center, the edges, and the corners of the field. The values of $W_F(\boldsymbol{\theta})$ at these nine points are derived from Simpson's rule, so the mean-square residual phase error ϵ^2 that is computed from these nine weights is the Simpson's rule approximation to the residual phase variance averaged over the entire FOV. Natural or laser guide stars are located at the center and four corners of the field, and deformable mirrors are located conjugate to ranges 0 and 5 km along the telescope's line of sight. Adaptive-optics performance does not appear to be a strong function of guide-star location or deformable-mirror altitude, provided that each deformable mirror actuator couples into the wave-front-sensor measurements for at least one guide star.

Figures 18 and 19 plot long-exposure OTF's at three points in the field of view of this multiconjugate configuration. The OTF's for a system that comprises a single deformable mirror and one natural, on-axis guide star are also plotted for comparison. These results assume a 3-m-

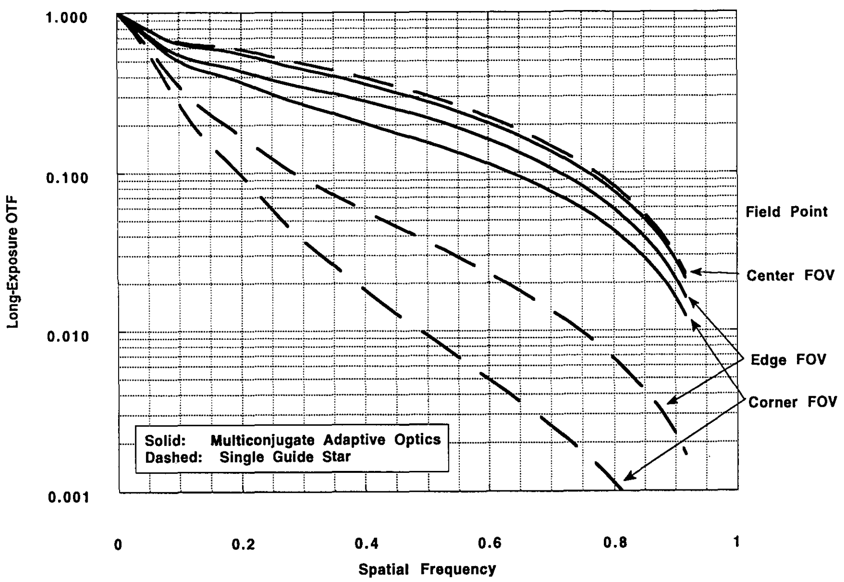

Fig. 18. Long-exposure OTF's for a multiconjugate configuration with five natural guide stars. These results assume the parameter values $D = 3$ m, $L = 0.25$ m, $\psi = 0°$, and $\lambda = 0.5$ μm and the atmospheric profiles illustrated in Figs. 3 and 4. Deformable mirrors are located conjugate to altitudes of 0 and 5 km, and the interactuator spacing is 0.25 m for both mirrors. These results also assume zero wave-front-sensor measurement noise and an infinite control-loop bandwidth.

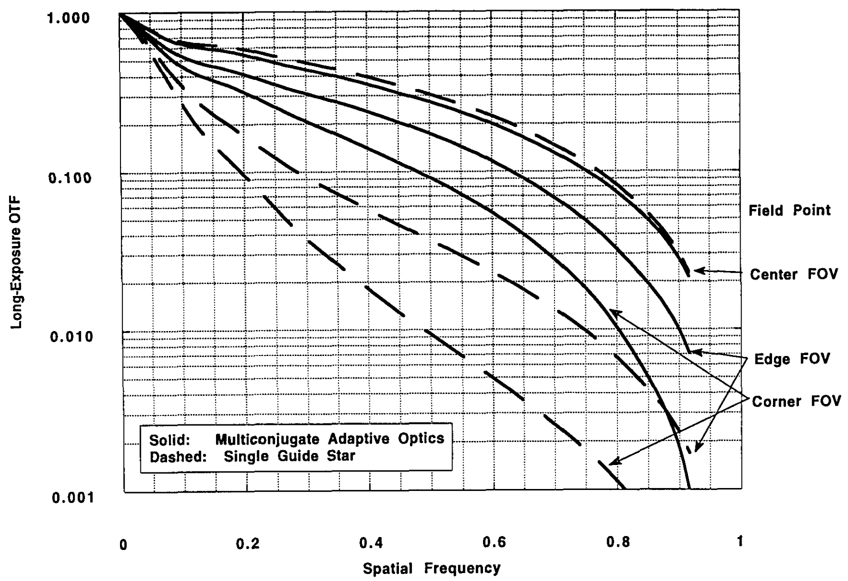

Fig. 19. Long-exposure OTF's for a multiconjugate configuration with one on-axis natural guide star and four mesospheric-sodium guide stars. This figure is similar to Fig. 18, except that the four natural guide stars at the corners of the telescope's FOV have been replaced by guide stars in the mesospheric sodium layer.

aperture diameter, a 0° zenith angle, $D/L = 12$ for both deformable mirrors, the Fried subaperture geometry for all wave-front sensors, a 0.5-μm evaluation wavelength, zero wave-front-sensor measurement noise, an infinite control-loop bandwidth, and the atmospheric $C_n^2(h)$ profile that is illustrated in Fig. 3. Figure 18 plots results for five natural guide stars, and Fig. 19 describes system performance with one natural and four mesospheric sodium-layer guide stars. Because the isoplanatic angle for this wavelength and this turbulence profile is ~20 μrad, the OTF's for a single guide star are degraded considerably at the edge and the corners of the ±50-μrad FOV. The long-exposure Strehl ratios corresponding to these OTF's are 0.774 (center), 0.140 (edge), and 0.070 (corner). The OTF's for either of the two multiconjugate configurations decrease much more gradually with field angle. The long-exposure Strehl ratios for these OTF's are 0.720/0.704 (center), 0.569/0.447 (edge), and 0.441/0.282 (corner), with the first number of each pair corresponding to the configuration with five natural guide stars.

The effect of a finite servo bandwidth and wave-front-sensor measurement noise on the performance of this multiconjugate adaptive optics system is listed in Table 2. The results are listed for control-loop bandwidths f between 10 and 60 Hz and rms wave-front-sensor noise levels from 0.00 to 0.20 wave at $10f$. Table 2 is for the case of five natural guide stars, with all the remaining system parameters as for Fig. 18. The relative reduction to long-exposure Strehl ratio resulting from a finite servo bandwidth with zero wave-front-sensor noise is relatively uniform for all three field points that are evaluated and is approximately equal to the on-axis Strehl-ratio reduction for a system that uses only a single guide star. Wave-front-sensor noise actually has a lesser effect on the multiconjugate system than on the single guide star system, presumably because the use of multiple guide stars introduces some redundancy into the sensor measurement vector. The increased complexity of the multiconjugate wave-front reconstruction algorithm evidently does not imply increased sensitivity to wave-front-sensor noise or servo lag.

5. SUMMARY

The impulse-response function of a linear closed-loop adaptive-optics system can be a highly nonlinear function of the wave-front reconstruction matrix. This relationship is linear for reconstructors that precisely predict

Table 2. Relative Reductions in Long-Exposure Strehl Ratio Resulting from Finite Servo Bandwidth (f) and Sensor Noise Level for a Multiconjugate Adaptive-Optics System[a]

Noise at $10f$, Waves	Single Guide Star On Axis	Multiconjugate Adaptive Optics On Axis	Multiconjugate Adaptive Optics Edge FOV	Multiconjugate Adaptive Optics Corner FOV
$f = 60$ Hz				
0.00	0.943	0.942	0.953	0.955
0.05	0.919	0.924	0.937	0.950
0.10	0.867	0.892	0.909	0.937
0.20	0.702	0.806	0.826	0.864
$f = 40$ Hz				
0.00	0.885	0.885	0.902	0.907
0.05	0.862	0.868	0.886	0.902
0.10	0.814	0.837	0.859	0.889
0.20	0.659	0.757	0.784	0.821
$f = 30$ Hz				
0.00	0.818	0.818	0.840	0.848
0.05	0.796	0.803	0.826	0.844
0.10	0.752	0.775	0.801	0.832
0.20	0.611	0.703	0.731	0.769
$f = 20$ Hz				
0.00	0.677	0.679	0.707	0.721
0.05	0.660	0.667	0.696	0.719
0.10	0.624	0.644	0.677	0.707
0.20	0.509	0.585	0.617	0.655
$f = 10$ Hz				
0.00	0.346	0.351	0.380	0.404
0.05	0.339	0.346	0.374	0.403
0.10	0.323	0.336	0.366	0.397
0.20	0.270	0.308	0.337	0.372

[a]These results assume the parameter values $\lambda = 0.5$ μm, $D = 3$ m, $D/L = 12$ and the atmospheric conditions given in Figs. 3 and 4. The multiconjugate adaptive-optics configuration is described in Fig. 17 and in the text.

the deformable-mirror actuator command vector in the absence of wave-front-sensor noise and atmospheric turbulence. The closed-loop performance of such reconstructors can be evaluated and optimized with minimal-variance estimation techniques that have previously been applied to the open-loop case.[7,12] The results that were obtained describe adaptive-optics system performance in the presence of error sources, including fitting error, sensor noise, servo lag, and anisoplanatism. They are also applicable to multiconjugate adaptive-optics configurations that incorporate multiple guide stars and deformable mirrors to compensate atmospheric turbulence across an extended field of view.

APPENDIX A: $Q_* Q = Q_*$

Section 2 of this paper requires the relationship $Q_* Q = Q_*$, where the matrix Q is an arbitrary orthogonal projection operator that is defined on the vector space of deformable-mirror actuator commands and the projection operator Q_* is defined by Eqs. (2.38)–(2.40). Since both of these matrices are orthogonal projection operators, we may prove this equality by demonstrating that the null space of Q is contained within the null space of Q_*. Suppose that the vector $\mathbf{x}$ is an element of the null space of Q so that $Q\mathbf{x} = 0$. Using Eqs. (2.18), (2.33), (2.34), and the condition $Q^T R = RQ$ for the orthogonal projection operator Q yields the relationship

$$\mathbf{x}^T R^{1/2} O^T \Lambda O R^{1/2} \mathbf{x} = \mathbf{x}^T (RMA^T + AM^T R + RMSM^T R)\mathbf{x} = 0. \tag{A1}$$

The vector $R^{1/2}\mathbf{x}$ is therefore an eigenvector of the matrix $O^T \Lambda O$, with eigenvalue 0. Equations (2.38) and (2.39) for the matrix L imply that

$$O^T L O R^{1/2} \mathbf{x} = 0, \tag{A2}$$

which, when combined with Eq. (2.40), yields

$$Q_* \mathbf{x} = 0. \tag{A3}$$

The vector $\mathbf{x}$ is therefore contained in the null space of the matrix Q_*, which is sufficient to demonstrate that $Q_* Q = Q_*$.

APPENDIX B: EVALUATION OF $f(a,b)$

The function $f(a, b)$ is defined in Section 3 by the integral

$$f(a,b) = \int_0^\infty \mathrm{d}\nu \nu^{-8/3} J_0(a\nu)[J_0(b\nu) - 1]. \tag{B1}$$

Here J_0 is a Bessel function of the first kind.[25] This appendix derives a computational formula for $f(a, b)$ in terms of the gamma function and the hypergeometric functions.

Integrating Eq. (B1) by parts yields

$$\begin{aligned} f(a,b) = &-\frac{3}{5}\nu^{-5/3} J_0(a\nu)[J_0(b\nu) - 1]\Big|_0^\infty \\ &+ \frac{3}{5}\int_0^\infty \mathrm{d}\nu \nu^{-5/3}[aJ_1(a\nu) - aJ_1(a\nu)J_0(b\nu) \\ &- bJ_1(b\nu)J_0(a\nu)]. \end{aligned} \tag{B2}$$

The first term on the right-hand side of Eq. (B2) vanishes because of the asymptotic behavior of the function J_0. The second term may be abbreviated in the form

$$f(a,b) = \frac{3}{5}[ag(0,a) - ag(b,a) - bg(a,b)], \tag{B3}$$

where the function $g(a, b)$ is defined by

$$g(a,b) = \int_0^\infty \mathrm{d}\nu \nu^{-5/3} J_0(a\nu) J_1(b\nu). \tag{B4}$$

This integral can be evaluated with Eqs. (11.4.33) and (11.4.34) of Luke[30] with the following result:

$$g(a,b) = \begin{cases} \dfrac{a^{2/3}}{2^{5/3}} \dfrac{\Gamma(1/6)}{\Gamma(11/6)} \left(\dfrac{b}{a}\right)^{2/3} {}_2F_1\left[\dfrac{1}{6}, -\dfrac{5}{6}; 1; \left(\dfrac{a}{b}\right)^2\right] & \text{if } a \le b \\ \dfrac{a^{2/3}}{2^{5/3}} \dfrac{\Gamma(1/6)}{\Gamma(5/6)} \left(\dfrac{b}{a}\right) {}_2F_1\left[\dfrac{1}{6}, \dfrac{1}{6}; 2; \left(\dfrac{b}{a}\right)^2\right] & \text{otherwise} \end{cases}, \tag{B5}$$

where ${}_2F_1(a, b; c; z)$ is a hypergeometric function.[31]

Equations (B3) and (B5) provide the desired computational formula for the function $f(a, b)$. Direct numerical evaluation of the definition[31]

$${}_2F_1(a,b;c;z) = \frac{\Gamma(c)}{\Gamma(a)\Gamma(b)} \sum_{n=0}^\infty \frac{\Gamma(a+n)\Gamma(b+n)}{\Gamma(c+n)} \frac{z^n}{n!} \tag{B6}$$

can require a very large number of terms for values of z approaching unity. It is much more efficient to precompute the values and the derivatives of the hypergeometric function with Eq. (15.2.1) of Oberhettinger[31] at a set of points within the unit interval and then to compute, with Taylor series approximations, all the remaining hypergeometric evaluations that are necessary for Eq. (B5). Fifth-order derivatives precomputed at 40 points provide 11 digits of accuracy for this purpose.

APPENDIX C: NUMERICAL INTEGRATIONS

The evaluation formulas that are derived in Section 3 for the quantities $\langle \epsilon_0^2 \rangle$, A, and S include integrals over the field of view of the telescope, the aperture of the telescope, the range, and the time. This appendix briefly summarizes the numerical techniques that are used to compute these integrals.

The integral with respect to range in Eq. (3.27) is evaluated with a Gaussian quadrature formula[32] of the form

$$\int_0^\infty \mathrm{d}z C_n^2(z) f(z) \approx \sum_{i=0}^M c_i f(z_i). \tag{C1}$$

The coefficients c_i and ranges z_i are selected to satisfy the conditions

$$\int_0^\infty \mathrm{d}z C_n^2(z) z^m = \sum_{i=0}^M c_i z_i^m \tag{C2}$$

Table 3. Gaussian Quadrature Weights, Altitudes, and Wind Speeds for Altitude Integrations Weighted by $C_n^2(z)$

Layer	Altitude (m)	Turbulence Weight	Wind Speed (m/s)
1	61.211	0.216	7.997
2	1178.485	0.105	9.760
3	2350.632	0.415	9.280
4	4567.710	0.078	28.119
5	7158.162	0.064	28.286
6	11763.788	0.032	17.946
7	14947.749	0.027	9.126
8	17632.778	0.022	4.926
9	21184.678	0.006	4.071
10	23528.705	0.003	2.519
11	24864.313	0.001	2.301

Table 4. Discrete Weights for Temporal Integrals Weighted by $k[\exp(-k\tau)]$

i	c_i
0	0.395
1	1.109
2	0.990
3	1.011
4	0.995
5	1.001
6	0.984
7	0.980
8	0.961
9	0.432
10	3.770

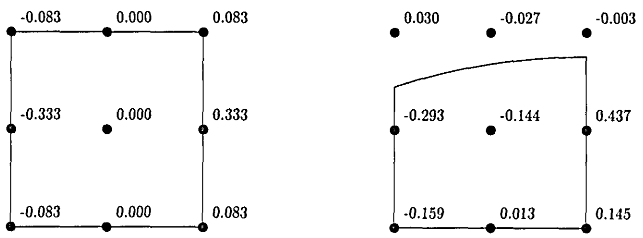

(a) (b)

Fig. 20. Discrete weights for x-wave-front slope measurements on (a) unobscured and (b) partially obscured wave-front-sensor subapertures. The phase values at the nine points are summed with the indicated weights to approximate the average x-wave-front tilt over the continuous subaperture. This approximation is exact for any wave-front quadratic in both x and y over the square that is bounded by the four corner points.

for $m \leq 2M - 1$. Values of c_i and z_i for the turbulence profiles that are used in Section 4 and for $M = 11$ are listed in Table 3.

The temporal integral in Eq. (3.27) is approximated with the discrete summation

$$\int_0^\infty \mathrm{d}\tau w(\tau) f(t - \tau) \approx \sum_{i=0}^{M} w(i\Delta\tau) c_i \Delta\tau f(t - i\Delta\tau). \qquad \text{(C3)}$$

The coefficients c_i are in this case selected to minimize the mean-square error

$$e^2 = \left\langle \left[\int_0^\infty \mathrm{d}\tau \phi(\mathbf{x}, \boldsymbol{\theta}, t - \tau) w(\tau) - \sum_{i=0}^{M} \phi(\mathbf{x}, \boldsymbol{\theta}, t - i\Delta\tau) w(i\Delta\tau) c_i \Delta\tau \right] \right\rangle \qquad \text{(C4)}$$

for the Kolmolgorov spectrum with an infinite outer scale and a zero inner scale. We recall from Eq. (3.10) that the possible values for the temporal weighting function $w(\tau)$ are either $\delta(\tau)$ or $k[\exp(-k\tau)]$. If $w(\tau) = \delta(\tau)$, the required weighting coefficients are clearly $M = 0$ and $c_0 = 1$. For the case $w(\tau) = k[\exp(-k\tau)]$ we use the parameters $M = 10$, $\Delta\tau = 1/(2k)$, and the values of c_i that are listed in Table 4. The final coefficient c_{10} is larger than the remaining coefficients to account for truncated portion of the integral in relation C3.

Finally, the spatial integrals in Eqs. (3.18)–(3.20) and (3.27) are approximated with two-dimensional discrete summations of the form

$$\int \mathrm{d}\mathbf{x} v(\mathbf{x}) f(\mathbf{x}) \approx \sum_{i,j} v_{ij} f(i\Delta x, j\Delta x). \qquad \text{(C5)}$$

The grid-point spacing Δx is equal to one half of the spacing between deformable-mirror actuators on the deformable mirror with the highest actuator density. The coefficients v_{ij} are chosen so that relation (C5) is an equality for any function f that is second order in both x_1 and x_2 within each square that is bounded by four of these actuators. For example, Fig. 20(a) illustrates the coefficients that are used to compute the x-wave-front slope on a completely illuminated wave-front-sensor subaperture. These are standard Simpson's rule weights. Figure 20(b) illustrates the modified coefficients that are used for a subaperture that is partially obscured by the edge of the telescope aperture. These coefficients yield the exact wave-front tilt for any wave-front that is quadratic in both x_1 and x_2 within the area that is bounded by the four actuators.

ACKNOWLEDGMENTS

This research was initiated under U.S. Air Force contract F29601-87-C-0005 while the author was employed at Logicon R & D Associates. I gratefully acknowledge useful conversations concerning multiconjugate adaptive-optics systems with D. Johnston and B. M. Welsh. R. Pringle, R. F. Fugate, and M. P. Jelonek read early drafts of this manuscript and provided many helpful suggestions.

REFERENCES AND NOTES

1. R. Q. Fugate, D. L. Fried, G. A. Ameer, B. R. Boeke, S. L. Browne, P. H. Roberts, R. E. Ruane, G. A. Tyler, and L. M. Wopat, "Measurement of atmospheric wave-front distortion using scattered light from a laser guide-star," Nature (London) **353,** 144–146 (1991).
2. C. A. Primmerman, D. V. Murphy, D. A. Page, B. G. Zollars, and H. T. Barclay, "Compensation of atmospheric optical distortion using a synthetic beacon," Nature (London) **353,** 141–143 (1991).
3. J. F. Belsher and D. L. Fried, "Expected antenna gain when correcting tilt-free wavefronts," Rep. TR-576 (Optical Sciences Company, Placentia, Calif., 1984).
4. M. Welsh, "Imaging performance analysis of adaptive telescopes using laser guide stars," Appl. Opt. **30,** 5021–5030 (1991).

5. D. L. Fried, "Anisoplanatism in adaptive optics," J. Opt. Soc. Am. **72,** 52–61 (1982).
6. R. Foy and A. Labeyrie, "Feasibility of adaptive telescopes using laser probe," Astron. Astrophys. **152,** 129–131 (1985).
7. B. M. Welsh and C. S. Gardner, "Effects of turbulence-induced anisoplanatism on the imaging performance of adaptive-astronomical telescopes using laser guide stars," J. Opt. Soc. Am. A **8,** 69–80 (1991).
8. J. M. Beckers, "Increasing the size of the isoplanatic patch within multiconjugate adaptive optics," in *Proceedings of European Southern Observatory Conference and Workshop on Very Large Telescopes and Their Instrumentation,* M.-H. Ulrich, ed., Vol. 30 of ESO Conference and Workshop Proceedings (European Southern Observatory, Garching, Germany, 1988), pp. 693–703.
9. D. Johnston and B. Welsh, "Estimating contributions of turbulence layers to total wave-front phase aberration," in *Atmospheric Propagation and Remote Sensing,* A. Kohnle and W. B. Miller, eds., Proc. Soc. Photo-Opt. Instrum. Eng. **1688,** 510–521 (1992).
10. F. Roddier, M. Northcott, and J. E. Graves, "A simple low-order adaptive optics system for near-infrared applications," Publ. Astron. Soc. Pac. **103,** 131–149 (1991).
11. R. Hudgin, "Wave-front compensation error due to finite corrector-element size," J. Opt. Soc. Am. **67,** 393–396 (1977).
12. E. P. Wallner, "Optimal wave-front correction using slope measurement," J. Opt. Soc. Am. **73,** 1771–1776 (1983).
13. D. L. Fried, "Least-squares fitting a wave-front distortion estimate to an array of phase difference measurements," J. Opt. Soc. Am. **67,** 370–375 (1977).
14. R. H. Hudgin, "Wave-front reconstruction for compensated imaging," J. Opt. Soc. Am. **67,** 375–378 (1977).
15. J. Herrmann, "Least-squares wave-front errors of minimum norm," J. Opt. Soc. Am. **70,** 28–35 (1980).
16. D. P. Greenwood and D. L. Fried, "Power spectra requirements for wave-front compensation systems," J. Opt. Soc. Am. **66,** 193–206 (1976).
17. G. A. Tyler, "Turbulence-induced adaptive-optics performance evaluation: degradation in the time domain," J. Opt. Soc. Am. A **1,** 251–262 (1984).
18. Equations (2.1) and (2.2) imply that all modes of the wave-front-distortion profile must be compensated at the same control bandwidth. This simplification corresponds to the limitations of the existing closed-loop adaptive-optics systems with which we are familiar (see Ref. 1). More general approaches are possible but are not considered here.
19. This objective represents a departure from previous studies of reconstruction algorithms for multiconjugate systems (see Ref. 9), which have instead developed reconstructors to estimate the contributions of individual atmospheric-turbulence layers to the total wave-front-distortion profile.
20. Associated solutions for Λ and γ are $\Lambda = RQ(I - R^{-1}AS^{-1}G)(G^T s^{-1}G)^{-1}$ and $\gamma = A$. These solutions are not unique, since the matrix $(Q^T - I)$ is singular.
21. The square root $R^{1/2}$ of a symmetric, positive-definite matrix R is the quantity $O^T\Lambda^{1/2}O$, where the rows of the unitary matrix O are the eigenvectors of R and Λ is a diagonal matrix formed from the corresponding (positive) eigenvalues.
22. J. W. Hardy, "Active optics: a new technology for the control of light," Proc. IEEE **66,** 651–697 (1978).
23. R. J. Sasiela, "A unified approach to electromagnetic wave propagation in turbulence and the evaluation of multiparameter integrals," MIT Lincoln Lab. Tech. Rep. 807 (Massachusetts Institute of Technology, Cambridge, Mass., 1988).
24. B. M. Welsh and C. S. Gardner, "Performance analysis of adaptive-optics systems using slope sensors," J. Opt. Soc. Am. A **6,** 1913–1923 (1989).
25. F. Olver, "Bessel functions of integer order," in *Handbook of Mathematical Functions,* M. Abramowitz and I. Stegun, eds. (Dover, New York, 1973), pp. 358–389.
26. D. L. Fried, "Limited resolution looking down through the atmosphere," J. Opt. Soc. Am. **56,** 1380–1384 (1966).
27. R. R. Beland, J. H. Brown, R. E. Good, and E. A. Murphy, "Optical turbulence characterization of AMOS," Rep. AFGL-TR-88-0153 (Air Force Geophysics Laboratory, Hanscom Air Force Base, Mass., 1989).
28. D. P. Greenwood, "Bandwidth specifications for adaptive optics systems," J. Opt. Soc. Am. **67,** 390–392 (1977).
29. J. Bahcall and R. Soniera, Astrophys. J. Suppl. **47,** 357 (1981).
30. Y. Luke, "Integrals of Bessel functions," in *Handbook of Mathematical Functions,* M. Abramowitz and I. Stegun, eds. (Dover, New York, 1973), pp. 479–494.
31. F. Oberhettinger, "Hypergeometric functions," in *Handbook of Mathematical Functions,* M. Abramowitz and I. Stegun, eds. (Dover, New York, 1973), pp. 555–566.
32. W. H. Press, B. P. Flannery, S. A. Teukolsky, and W. T. Vetterling, *Numerical Recipes* (Cambridge U. Press, Cambridge, 1987).